

Emission from multiple molecular isotopologues in a high-inclination protoplanetary disk

COLETTE SALYK,¹ KLAUS M. PONTOPPIDAN,^{2,3} ANDREA BANZATTI,⁴ EDWIN BERGIN,⁵ NICOLE ARULANANTHAM,⁶ JOAN NAJITA,⁷
GEOFFREY A. BLAKE,³ JOHN CARR,⁸ KE ZHANG,⁹ AND CHENGYAN XIE¹⁰

¹Vassar College, 124 Raymond Avenue, Poughkeepsie, NY 12604, USA

²Jet Propulsion Laboratory, California Institute of Technology, 4800 Oak Grove Drive, Pasadena, CA 91109, USA

³Division of Geological and Planetary Sciences, California Institute of Technology, MC 150-21, Pasadena, CA 91125, USA

⁴Department of Physics, Texas State University, 749 N Comanche Street, San Marcos, TX 78666, USA

⁵Department of Astronomy, University of Michigan, 1085 S. University, Ann Arbor, MI 48109, USA

⁶Space Telescope Science Institute, 3700 San Martin Drive, Baltimore, MD 21218, USA

⁷NSF's NOIRLab, 950 N. Cherry Avenue, Tucson, AZ 85719, USA

⁸Department of Astronomy, University of Maryland, 4296 Stadium Dr., College Park, MD 20742, USA

⁹Department of Astronomy, University of Wisconsin-Madison, Madison, WI 53706, USA

¹⁰Lunar and Planetary Laboratory, The University of Arizona, Tucson, AZ 85721, USA

ABSTRACT

We present a MIRI-MRS spectrum of the high-inclination protoplanetary disk around the solar-mass (K0) star MY Lup, obtained as part of the JWST Disk Infrared Spectral Chemistry Survey (JDISCS). The spectrum shows an unusually weak water emission spectrum for a disk around a star of its spectral type, but strong emission from CO₂, HCN, and isotopologues of both molecules. This includes the first ever detection of C¹⁸O¹⁶O and H¹³CN in an inner disk, as well as tentative detections of C¹⁷O¹⁶O and HC¹⁵N. Slab modeling provides molecular temperatures, column densities and emitting areas of the detected molecules. The emitting molecular gas is cold compared to that of other observed protoplanetary disk spectra. We estimate the isotopologue ratios of CO₂ and HCN, albeit with significant uncertainty. We suggest that the unusual spectrum of MY Lup arises from a combination of inner disk clearing, which removes emission from warm water, and its nearly edge-on inclination, which enhances line-of-sight column densities, although unusual chemistry may also be required. MY Lup's spectrum highlights the potential to detect and measure trace isotopologues to study isotopic fractionation in protoplanetary disks; observations at higher spectral resolving power is needed to constrain the isotopologue ratios to greater precision.

1. INTRODUCTION

The observational study of protoplanetary disk chemistry in the few AU region was set in motion by the discovery of a forest of molecular emission lines (Carr & Najita 2008; Salyk et al. 2008) using the Spitzer InfraRed Spectrograph (Spitzer-IRS; Houck et al. 2004). That work detected and characterized the emitting properties of several simple molecules including water, HCN, C₂H₂, CO₂ and OH (Carr & Najita 2011), and allowed for basic accounting of key atomic species O, C and N in the inner disk (Pontoppidan et al. 2010).

However, *cosmochemistry* in a solar system context often depends on a close attention to isotopic ratios. In the solar system, isotopic uniformity of many heavier refractory elements suggest substantial mixing prior to the formation of most planetary building blocks (e.g. Zhu et al. 2001; Moynier et al. 2009; Pringle et al. 2013). But small heterogeneities, especially of the volatile “CHON” atoms, tell

a more complex story. Each CHON atom may have a distinct isotopic history, including mixing between primordial reservoirs influenced by stellar nucleosynthesis and more processed solar-system materials, plus combinations of mass-dependent and mass-independent fractionation during early solar system evolution. Isotope ratios are often distinct for certain classes of solar system objects, such that they can be used to trace back the origins of a given object's volatiles (e.g. Bockelée-Morvan et al. 2015; Lis et al. 2013).

Hydrogen, as measured primarily in water, shows enhancement in D/H in comets as compared to the protosolar value and some planetary materials, reflecting possible inheritance of materials deuterated in the cold interstellar medium (ISM; Bockelée-Morvan et al. 2015). Earth also has a relatively high D/H ratio, suggesting a possible outer solar system contribution to its water reservoir (e.g. Bockelée-Morvan et al. 2015). Nitrogen, as measured in CN and HCN, shows a rough trend of increased enhancement in heavier ¹⁵N from the protosolar value, to inner solar system bodies, and then to outer solar system bodies, like comets (Marty 2012). Carbon shows a wide range of ¹³C/¹²C ratios as measured in presolar grains, likely reflecting pollution by extraterrestrial materials

influenced by nucleosynthetic processes (Karhu & Bekker 2023). Other solar system materials show much smaller heterogeneities, reflecting some enhancement of ^{13}C relative to the bulk solar value (Karhu & Bekker 2023).

Oxygen isotope ratios lie on a distinct slope-1 mass-independent fractionation line in a three-isotope ($^{17}\text{O}/^{16}\text{O}$ vs. $^{18}\text{O}/^{16}\text{O}$) plot (e.g., Clayton et al. 1973; McKeegan et al. 2011). This may be caused by enhanced photodissociation of C^{17}O and C^{18}O relative to C^{16}O , due to C^{16}O self-shielding, followed by subsequent incorporation of ^{17}O and ^{18}O into water ice (Thiemens & Heidenreich 1983; Yurimoto & Kuramoto 2004; Lyons & Young 2005).

It is not yet clear to what extent the complex isotopic histories of solar nebula materials translate to other protoplanetary disks, but models and observations of isotopologues in outer disks provide some insight. Disk models suggest that there should be a range of isotopic ratios varying as a function of both disk location and the nature of the specific molecules, due to such factors as the local UV radiation field, the effectiveness of grain shielding, and the extent to which a formation pathway for a given molecule comes from the isotopically “heavy” or “light” products of the dissociation process (e.g. Miotello et al. 2014). Nitrogen isotopes observed with ALMA in HCN and CN show evidence that CN may arise from reservoirs unaffected by isotope-selective photodissociation (Hily-Blant et al. 2017), while HCN may, in some parts of the disk, have isotopic enhancements due to selective photodissociation (Hily-Blant et al. 2019). Similarly, ALMA observations of C_2H and CO suggest that the two molecules arise from different isotopic reservoirs (Bergin et al. 2024), and that the CO isotopic ratios are radius-dependent (Yoshida et al. 2022). Precise measurements of all oxygen isotopes in disks are challenging, but Smith et al. (2009) used infrared absorption spectroscopy of an outer protoplanetary disk to measure three oxygen CO isotopologues and found enrichment of C^{18}O and C^{17}O , consistent with selective photodissociation.

Observations of isotopic ratios in *inner* disks could be used to further test our fractionation hypotheses for the terrestrial planet forming-regions. They could also confirm whether radial gradients exist that could be used to trace back the origins of exo-planetary volatiles. However, since molecular carriers of rarer isotopes can be much less abundant than primary isotopologues, very high sensitivity infrared spectroscopy is needed to detect them.

The James Webb Space Telescope’s Mid-Infrared Instrument (Rieke et al. 2015) Medium Resolution Spectrometer (hereafter JWST MIRI-MRS; Wright et al. 2023) offers significant improvements in sensitivity to molecular emission compared to its predecessor, the Spitzer Infrared Spectrograph (Houck et al. 2004), primarily due to the telescope’s aperture size, but also enhanced by the improved resolving power. Therefore, JWST potentially offers a powerful new tool to identify and study less abundant molecules, including isotopologues (e.g. Grant et al. 2023; Xie et al. 2023). While MIRI-MRS does suffer from instrumental fringing, which can limit signal-to-noise ratios (SNR), this can be substan-

tially mitigated by using an asteroid as a “fringing calibrator” (Pontoppidan et al. 2024).

However, detection of infrared emission from rare species is still subject to a physical limitation: for protoplanetary disks observed in the infrared, the presence of dust limits the observable column of gas to the disk upper atmosphere. At least three conditions can lead to more favorable conditions to detecting isotopologues in emission. In a first, overall enhancement of a given molecule, for example due to radial transport of icy pebbles followed by sublimation (Bosman et al. 2017), will enhance the secondary/primary isotopologue line ratio as the molecular column density grows. In a second, rare species may be revealed if dust opacities are reduced due to physical clearing or grain growth, essentially increasing the gas column above the $\tau = 1$ surface. Such a scenario has been suggested by Grant et al. (2023), and further explored by Vlasblom et al. (2024) to explain a detection of $^{13}\text{CO}_2$ in the GW Lup disk. In a third possibility, presented in this work, a favorable geometry could enhance the observable gas column by allowing the observer to look through a less dusty upper part of the disk atmosphere.

In this work, we present MIRI-MRS observations of isotopologues of both CO_2 and HCN in the disk surrounding the young star MY Lup. MY Lup is a K0, solar-mass ($\log M_* = 0.09_{-0.12}^{+0.03}$) star (Alcalá et al. 2017; Andrews et al. 2018) with a disk inclination measured to be 73 ± 0.1 degrees at millimeter (mm) wavelengths (Huang et al. 2018), or 77 ± 1.5 in the near-infrared (Avenhaus et al. 2018). MY Lup’s Kepler lightcurve has characterized it as a so-called “dipper”, with shallow, frequent, semi-periodic dips in brightness likely due to occultation by the high-inclination disk (Bredall et al. 2020). Its disk shows possible evidence for inner clearing based on both infrared photometry (Romero et al. 2012) and mm-wave continuum imaging (van der Marel et al. 2018), although obscuration of the inner disk and star by the outer disk complicates interpretations of the interferometric data (Alcalá et al. 2019). Its accretion rate of $10^{-8} M_{\odot} \text{yr}^{-1}$ may be similar to that of other full disks of comparable mass (Romero et al. 2012; Alcalá et al. 2019), although accretion rates below $2 \times 10^{-10} M_{\odot} \text{yr}^{-1}$ were also reported by Alcalá et al. (2017). This source was also observed by the Atacama Large Millimeter/Submillimeter Array (ALMA) at high resolution as part of the The Disk Substructures at High Angular Resolution Project (DSHARP; Andrews et al. 2018). The ALMA images show shallow but detectable dark bands at ~ 50 and 190 AU, and bright rings at ~ 130 and 260 AU (Huang et al. 2018).

We use the detected CO_2 and HCN isotopologues to determine the properties (temperature, column density and emitting area) of the emitting molecules, and also place constraints on the $^{12}\text{C}/^{13}\text{C}$, $^{16}\text{O}/^{18}\text{O}$ and $^{16}\text{O}/^{17}\text{O}$ ratios in these molecules. In addition, we consider what scenario(s) could have caused this unique set of isotopologue detections in MY Lup.

2. DATA ACQUISITION AND REDUCTION

MY Lup was observed with MIRI-MRS as part of the Cycle 1 program 1584 (PIs: Salyk, Pontoppidan) on 2023 Aug 13. It was observed in all four channels with a 4-point dither pattern optimized for all channels, with a total exposure time of 1668 s. Raw data used in this paper can be found in MAST: [10.17909/rd5f-h484](https://mast.stsci.edu/portal/#/data/archive/10.17909/rd5f-h484). MY Lup was reduced using the standard procedure developed by the JWST Disk Infrared Spectral Chemistry Survey (JDISCS) team, a procedure fully described in [Pontoppidan et al. \(2024\)](#). The reduction procedure utilizes the standard MRS pipeline ([Bushouse et al. 2024](#)) up to stage 2b, which produces three-dimensional cubes for every exposure. For the data presented here, we used pipeline version 1.15.0 and Calibration Reference Data System context 1253. Our reduction procedure then deviates from the standard pipeline. In short, a set of wavelength-summed 2D images are created for each channel and subband to locate the source, and then 1D spectra are extracted with a wavelength-dependent aperture size. Each 1D spectrum is then divided by an “empirical spectral response function” derived from the fringe calibrator asteroid, and then combined together. Temporal changes in the fringing pattern imply that observations close in time usually yield the best fringe removal. For this set of observations, we used the asteroid 526 Jena, observed on 2023 Sep 21.

A continuum-subtracted spectrum was created following the procedure outlined in [Pontoppidan et al. \(2024\)](#)¹. It relies on the assumption that the continuum is produced by grains that emit blackbody emission plus broad solid-state features and, thus, that it can be approximated by the flux values between the much narrower gas-phase emission lines. To create the continuum spectrum, the original (line-rich) spectrum is first smoothed with a median filter of a specified box size (in this case, 41 pixels in width). Points in the original spectrum with flux values a certain threshold below the smoothed spectrum (in this case below a factor of 0.998) comprise the estimated continuum, and a new spectrum is created by interpolating between these continuum points. This procedure is repeated in an iterative fashion, in this case, for 10 iterations. The final continuum is then further smoothed with a second order Savitzky-Golay filter ([Savitzky & Golay 1964](#)) using the `scipy` ([Virtanen et al. 2020](#)) routine `savgol_filter` and is then subtracted from the original spectrum to produce the emission spectrum discussed in the remainder of this work.

3. SPECTRUM BASICS

The MIRI-MRS spectrum of MY Lup is shown in Figure 1, along with a continuum-subtracted spectrum. The typical SNR is ~ 300 based on line-free regions of the spectrum. The spectrum shows prominent emission from ionized Neon and Argon, neutral Sulfur, molecular and atomic Hydrogen, as well as CO₂, HCN and OH. HCN, CO₂ and OH emitting regions are highlighted as insets. Water vapor is also present in the spectrum, although features are less prominent than in

other T Tauri disk spectra (e.g. [Banzatti et al. 2023](#)). The unusual H I spectrum is explored further in Appendix A.

Unlike for MIRI-MRS spectra of other T Tauri disks (e.g. [Temmink et al. 2024a](#)), the spectrum shows no evidence for CO emission. Figure 2 shows instead that the $\sim 5 \mu\text{m}$ region has a spectral shape very similar to a spectrum of the weak-line T Tauri star TWA 7 — the best apparent match from a small sample of weak-line T Tauri stars observed with Keck-NIRSPEC². This suggests that at $\sim 5 \mu\text{m}$, the spectrum of MY Lup has detectable photospheric features and, therefore, low veiling (r , defined as the ratio of continuum to photospheric flux). Note that veiling increases with wavelength as the stellar photospheric flux drops, so photospheric features become less apparent at longer wavelengths. Based on the spectral scaling required to match the TWA 7 spectrum to the MY Lup spectrum, the M-band veiling would be $r_M \sim 4.5$. However, TWA 7 has a spectral type of M2V, and is therefore a poor spectral type match to MY Lup. An incorrect template will artificially increase the veiling value, so we consider the M-band veiling to be < 4.5 , in line with veiling values for known disks with inner clearings ([Salyk et al. 2009](#)). Low veiling has also recently been observed in the MIRI-MRS spectrum of the 30 Myr disk around WISE J044634.16–262756.1B, where it was also interpreted as evidence of inner disk dust depletion ([Long et al. 2025](#)).

Spatial images are shown in Figure 3. Images are constructed by summing spectral channels near the line of interest, and then subtracting a continuum image constructed from adjacent channels on either side of the line. The continuum image is also scaled to the same strength as the spectral sum, to isolate extended structures. In the figure, we also mask an inner working angle of $1 \times 1.22 \lambda/D$ around the star, and overplot the ALMA continuum from [Andrews et al. \(2018\)](#) as contours. As can be seen in Figure 3, the H₂ S(1) line shows subtle evidence for a bipolar wide-angle wind perpendicular to the disk major axis; these images will be analyzed further in [Pontoppidan et al. \(2025, in preparation\)](#). We see no evidence for spatially extended emission in [Ne II] nor in any of the molecular lines.

4. ANALYSIS OF MOLECULAR SPECTRA

4.1. Water

Water vapor emission is less prominent in MY Lup’s spectrum than in typical solar-like T Tauri stars (e.g. [Pontoppidan et al. 2010](#)), but a few emission lines are observed. Figure 4 shows the most prominent observed emission lines in the $\sim 17\text{--}24 \mu\text{m}$ regions, as well as the $7 \mu\text{m}$ region, in which prominent bending mode rovibrational emission lines are seen in other targets (e.g. [Banzatti et al. 2023](#)).

To model the water emission, we use the HITRAN database ([Gordon et al. 2022](#)) to identify pure rotational water emission lines; we omitted rovibrational emission

¹ Continuum determination routine is available at <https://github.com/pontoppi/ctool/>

² Spectrum obtained by G. Blake and available at <https://www.spexodisks.com/>

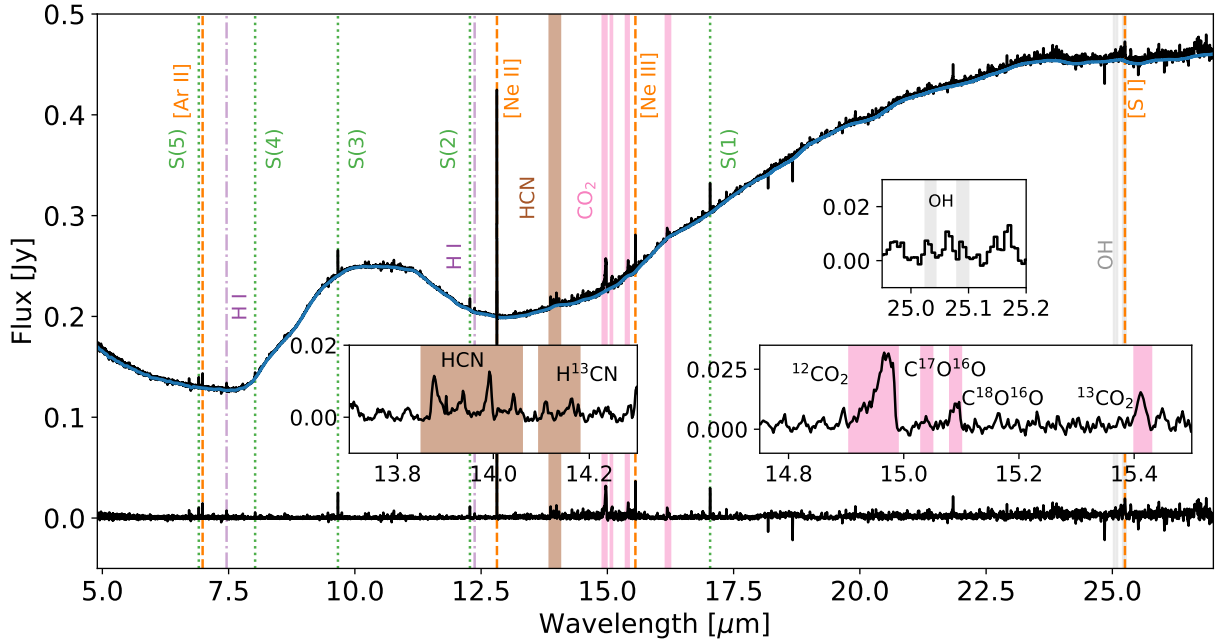


Figure 1. Observed MIRI-MRS spectrum of MY Lup (black, top), continuum fit (blue) and continuum-subtracted flux (black, bottom). Prominent atomic and molecular emission features are labeled; S(X) refers to H₂ 0-0 transitions. The broad feature at 10 μm is emission from solid silicates. Insets show continuum-subtracted spectra in the regions with significant HCN, CO₂ and OH emission; vertical bars also highlight locations of the main Q branches for different isotopologues.

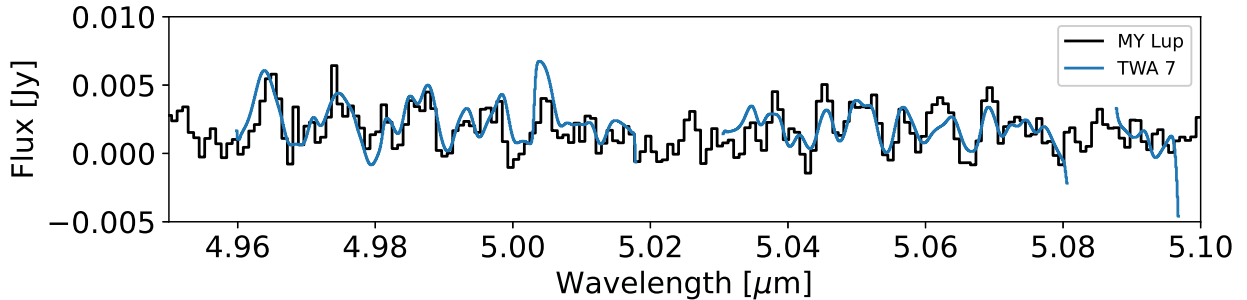


Figure 2. Continuum-subtracted MIRI-MRS spectrum of MY Lup (black) and Keck-NIRSPEC spectrum of weak-line T Tauri star TWA 7, convolved to a resolving power of $R=3000$ (blue) and scaled to visually match the MY Lup spectrum. Regions of the TWA 7 spectrum with high telluric contamination have been removed.

lines because their high critical densities likely result in non-Local Thermodynamic Equilibrium (non-LTE) excitation (Meijerink et al. 2009; Banzatti et al. 2023). We then use the “flux calculator” routine in the spectools-ir python package (Salyk 2022) to extract line fluxes. We visually vet the lines, ultimately selecting fluxes from 18 isolated lines to fit, ranging from 17–24 μm with excitation temperatures between ~ 1300 and 3600 K. We then fit the emission line fluxes with the spectools-ir “slab fitter” routine; this package performs Markov Chain Monte Carlo fitting with the “emcee” package (Foreman-Mackey et al. 2013) using flat priors and a “slab” emission model, which treats the gas as a

slab in LTE with a single temperature (T), column density (N , which need not be optically thin) and projected emitting area (A_{proj}). The projected emitting area can be converted to an emitting radius R if we assume a disk-like geometry, i.e., $A_{\text{proj}} = \pi R^2 \cos i$ where i is the disk inclination. Hereafter we take i to be the 77° near-infrared inclination from Avenhaus et al. (2018). Local line broadening is assumed to be thermal. We set the limits of our priors to 150–1000 K for T , 14–20 for $\log(N [\text{cm}^{-2}])$ and $-4 - 4$ for $\log A_{\text{proj}} [\text{AU}^2]$.

The MY Lup water vapor emission is found to be consistent with $T=336\pm 17$ K, $\log(N) = 18.00\pm 0.18$ ($N=9.9\times 10^{17} \text{cm}^{-2}$) and $R = 1.20 \pm 0.08$ AU (see also Table 1). The

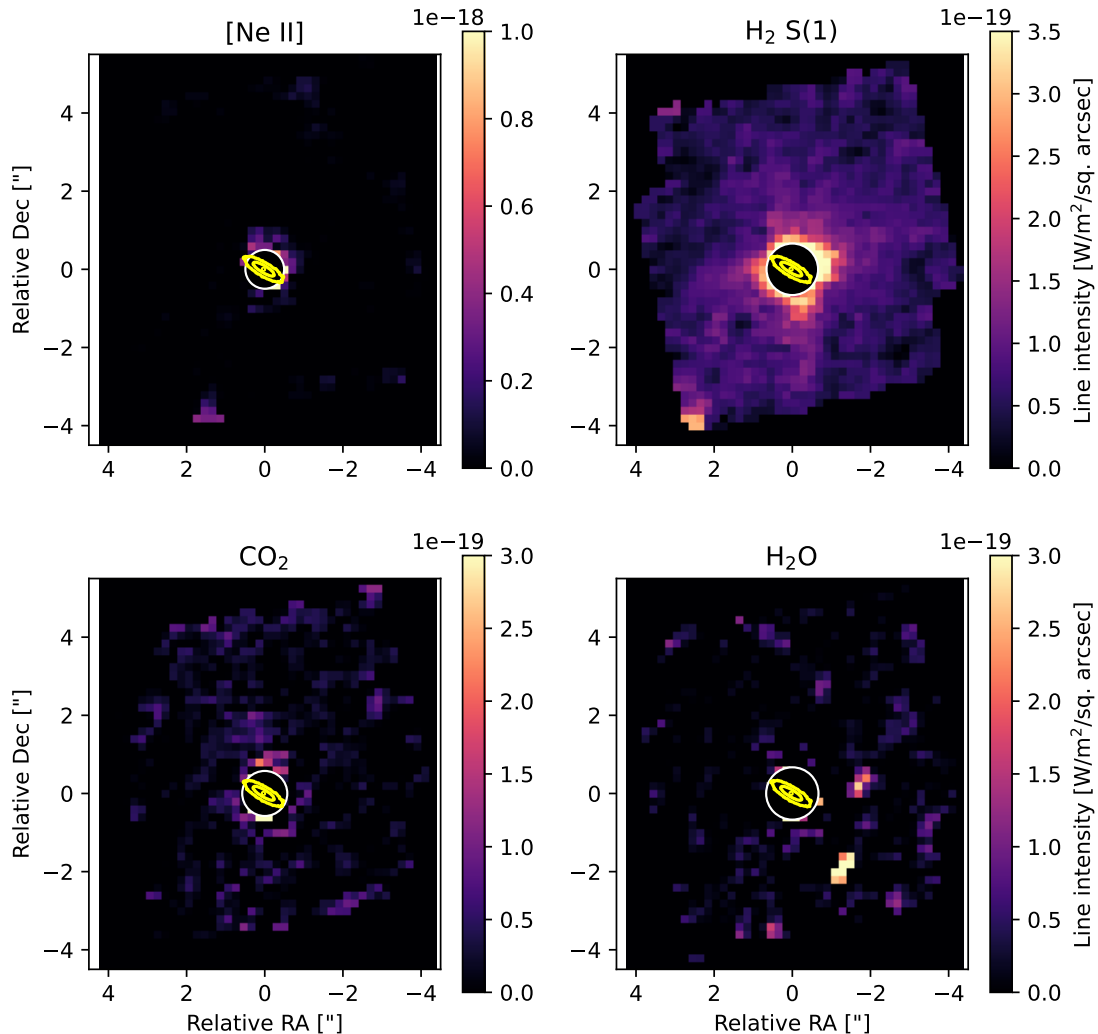


Figure 3. Line images of [Ne II], $\text{H}_2 \text{S}(1)$, $^{12}\text{CO}_2$ and a combination of 5 H_2O emission lines near $17 \mu\text{m}$. Circles mask an inner working angle of $1 \times 1.22 \lambda/D$ around the star. Yellow contours show the ALMA continuum from Andrews et al. (2018) (contours mark 5, 50 and 100σ).

best-fit emission model is shown in Figure 4; note that the rovibrational emission shown in the upper panel is not used in the fit due to the contribution of non-LTE excitation for these lines (Banzatti et al. 2024).

For subsequent analysis in this work, this best-fit water model is subtracted from the data to produce our nominal water-subtracted spectrum. In Figure 5, we show the impact of this water subtraction on the spectra in the HCN and CO_2 emitting regions. We note that there is minimal water contamination in the main Q branches of HCN, CO_2 and their isotopologues.

4.2. Carbon dioxide

Figure 6 shows the main CO_2 emitting region after subtraction of the best-fitting water model, along with CO_2 emission models, discussed below. The spectrum shows strong emission from CO_2 , as well as the isotopologues $^{13}\text{CO}_2$ and $\text{C}^{18}\text{O}^{16}\text{O}$. There is also marginal evidence for $\text{C}^{17}\text{O}^{16}\text{O}$, although this feature lies on top of a $^{12}\text{CO}_2$ P-branch line. ([Ne III] also emits at $15.555 \mu\text{m}$).

We then fit the CO_2 emission spectrum with LTE slab models using the spectools-ir “slabspec” routine (Salyk 2022). Unlike for the water emission, where isolated emission lines can be identified, and modeled and observed line fluxes can be compared, the CO_2 (and HCN) emission is highly blended, and a synthetic spectrum must be produced for

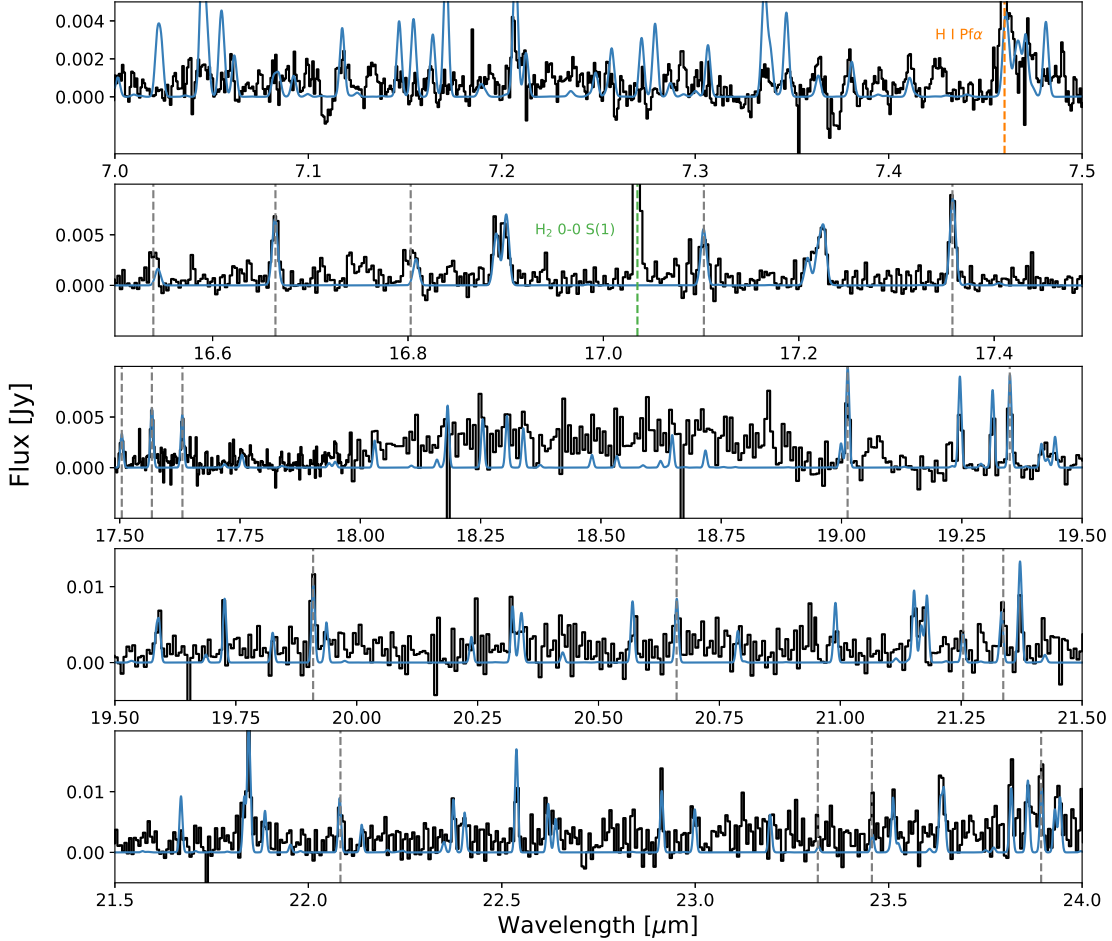


Figure 4. Portions of the continuum-subtracted MY Lup MIRI-MRS spectrum (black) and slab water emission model (blue) with $T=336$ K, $N=9.9 \times 10^{17} \text{ cm}^{-2}$, $R=1.20$ AU. Gray dashed lines mark locations of water lines used in the MCMC fit; note that rovibrational emission at 7μ is not included in the fit. H_2 and HI emission lines are also marked.

comparison with the observed data. Therefore, we explore parameter space with a less time-intensive grid of models (rather than MCMC). We create a grid of slab CO_2 emission models with a range of column densities (from 15–20 for $\log N [\text{cm}^{-2}]$ with $\Delta \log N = 0.2$) and temperatures (T from 200 K to 900 K with $\Delta T = 25$ K). For every CO_2 model, we adjust the model peak line fluxes to match the observed peaks, and then compute χ^2 . By adjusting the peak line flux values of the model, we are implicitly adding projected emitting area (A_{proj}) as a third model parameter (see, e.g. Grant et al. 2023). χ^2 is computed between 14.5 and 16.4 μm , excluding the $^{13}\text{CO}_2$, $\text{C}^{18}\text{O}^{16}\text{O}$, $\text{C}^{17}\text{O}^{16}\text{O}$ and [Ne III] emitting regions.

χ^2 contours are shown in Figure 7(a). White contours show 1, 2, and 3 sigma confidence intervals on the models,

assuming that the reduced $\chi^2 = 1$ for the best-fit model. The best-fit model has $T=575$ K, $N= 1.2 \times 10^{17} \text{ cm}^{-2}$ and $A_{\text{proj}} = 0.11 \text{ AU}^2$ ($R= 0.39 \text{ AU}$; see Table 1). However, there is a strong degeneracy between N and T . A closer look at the model fitting and residuals is provided in Figure 8. We see that multiple models can match the data in many regions, with only a few features dominating the differences in residuals. A close look at the residuals also shows that a feature on the red edge of the main CO_2 Q branch ($\sim 14.98 \mu\text{m}$) prefers low N models, while a feature at $\sim 16.2 \mu\text{m}$ prefers high N models. A $\sim 13.9 \mu\text{m}$ feature in the HCN-emitting region, which was excluded from the calculation of χ^2 due to contamination from HCN, also prefers the higher N models. The fact that different parts of the spectrum are consistent with different models may indicate contributions to the CO_2 spec-

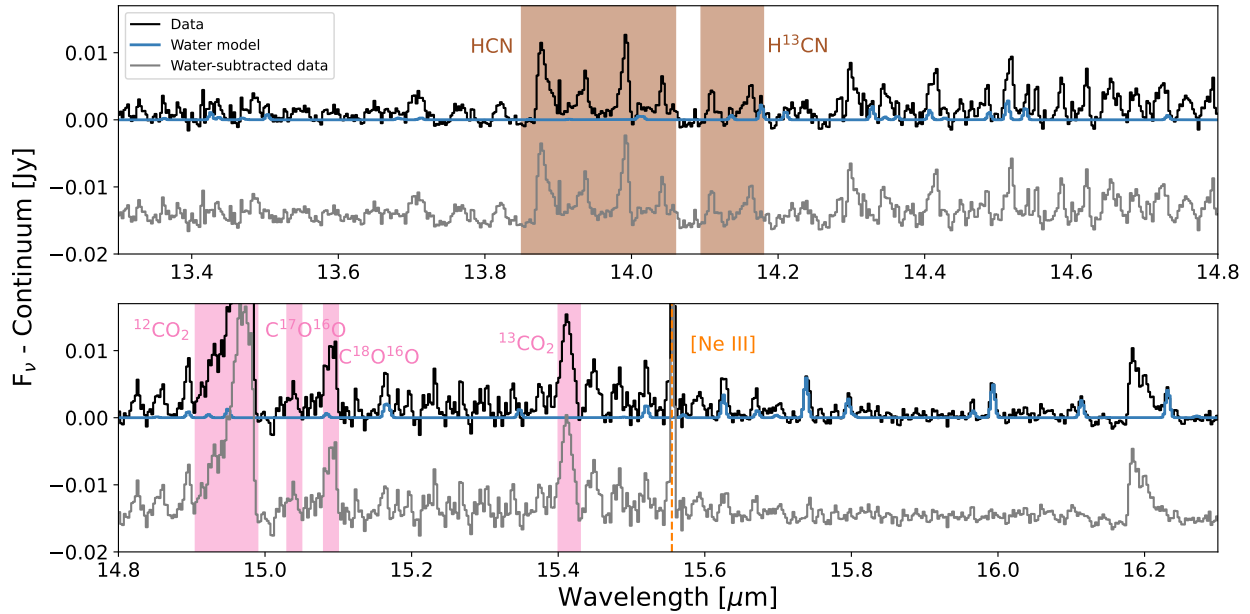


Figure 5. Observed continuum-subtracted MY Lup spectrum (black), best-fit slab water model convolved to a FWHM of 120 km s^{-1} (blue), and residuals (gray, offset) in the HCN and CO_2 -emitting regions. Vertical bars mark the same molecular Q branches highlighted in Figure 1.

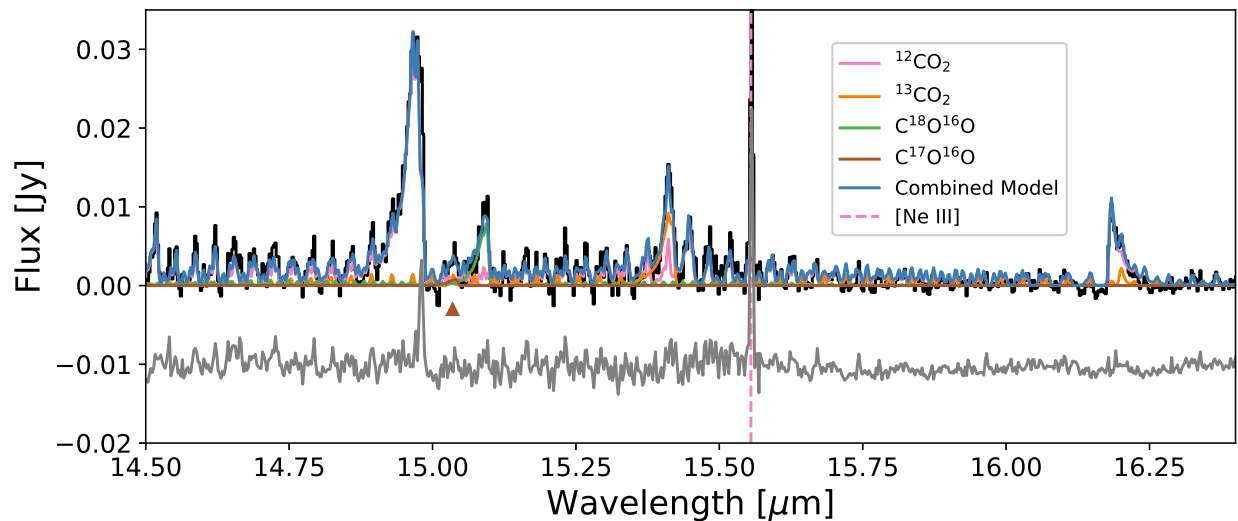


Figure 6. MY Lup MIRI-MRS continuum-subtracted and water model-subtracted spectrum in the CO_2 emitting region (black) plus slab emission models for CO_2 and isotopologues (various colors) assuming a C ratio fixed to the ISM value — see Table 1 for model parameters. The location of the marginal $\text{C}^{17}\text{O}^{16}\text{O}$ detection is highlighted with a brown triangle. $[\text{Ne III}]$ emission at $15.55 \mu\text{m}$ is also marked. Residuals (data - model) are shown in gray, offset by 0.01 Jy for clarity. The large residual at $\sim 14.99 \mu\text{m}$ is discussed further in Appendix B.

trum from non-LTE excitation, which we discuss further in Appendix B. Alternatively, the spectrum might be produced by disk regions with a range of temperatures and/or column densities.

A more stringent constraint on N can be provided by the relative strength of the Q branches for different isotopologues, *if* the abundance ratio of the two molecules is known and they are assumed to emit from the same reservoir. Although slightly different temperatures were required to fit

the $^{12}\text{CO}_2$ and $^{13}\text{CO}_2$ emission from GW Lup (Grant et al. 2023), we find no clear evidence that different temperatures are required to fit the two different Q branches in MY Lup’s spectrum. In panel (b) of Figure 7, we show the line peak ratio of the $^{12}\text{CO}_2$ and $^{13}\text{CO}_2$ Q branches assuming $^{12}\text{CO}_2/^{13}\text{CO}_2$ is set to the ISM $^{12}\text{C}/^{13}\text{C}$ abundance ratio of 68 (Milam et al. 2005, See also Table 2). The observed line peak ratio is 2.24 ± 0.24 , which implies $N_{\text{CO}_2} \gtrsim 10^{18} \text{ cm}^{-2}$ for this assumed molecular ratio. In panel (c), we

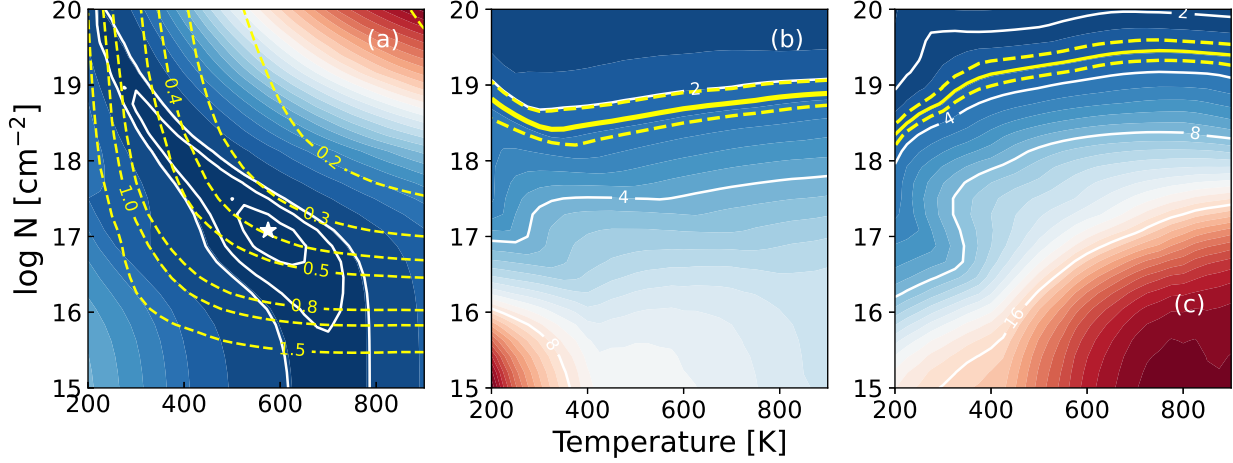


Figure 7. (a) χ^2 contour plot for fits to the CO₂ emission, as a function of temperature and CO₂ column density. White solid contour lines mark 1, 2, and 3-sigma confidence intervals on the best-fit model, shown with a white star. Dashed yellow lines show best-fit emitting radii (R) corresponding to each model as yellow dashed lines. (b) Line peak ratio of the Q branches of ¹²CO and ¹³CO, assuming ¹²C/¹³C = 68. Yellow lines show the observed ratio of 2.24 ± 0.24 . (c) Line peak ratio of the Q branches of ¹²CO and C¹⁸O¹⁶O, assuming ¹²CO/C¹⁸O¹⁶O = 278.5. Yellow lines show the observed ratio of 2.97 ± 0.36 .

Species	N [cm ⁻²]	T [K]	R [AU]	Ratio ^a	R _i /R _{ISM} ^b
H ₂ O	9.9×10^{17}	336	1.20		
¹² CO ₂ ^c	1.2×10^{17}	575	0.39		
¹² CO ₂	3.5×10^{18}	325	0.58	...	
¹³ CO ₂	5.1×10^{16}	"	"	68^d	1
C ¹⁸ O ¹⁶ O	1.8×10^{16}	"	"	381^{+132}_{-100}	$1.46^{0.52}_{-0.38}$
C ¹⁷ O ¹⁶ O	3.1×10^{15}	"	"	$> 2272_{-882}$	$< 0.88^{+0.56}$
¹² CO ₂	5.6×10^{18}	300	0.65	...	
¹³ CO ₂	7.3×10^{16}	"	"	77^{+84}_{-25}	$0.88^{+0.42}_{-0.46}$
C ¹⁸ O ¹⁶ O	2.0×10^{16}	"	"	557^c	1
C ¹⁷ O ¹⁶ O	3.6×10^{15}	"	"	$> 3109_{-1028}$	$< 0.64^{+0.32}$
HCN	1.4×10^{19}	250	0.61		
H ¹³ CN	2.0×10^{17}	"	"	68	

^aAtomic ratio of the main light isotope divided by the selected heavy isotope.

^bHere, following cosmochemistry conventions, R_i is the atomic ratio of the selected heavy isotope relative to the main isotope, i.e., the inverse of that used in the remainder of the text. R_i/R_{ISM} > 1 implies enhancement of the *heavier* isotope relative to ISM values.

^cFit including ¹²CO₂ only. See discussion of degeneracies in Section 4.2.

^dRatio fixed to the ISM value.

Table 1. Summary of slab model fits

Ratio	Value	Reference
¹² C/ ¹³ C	68	Milam et al. (2005)
¹⁶ O/ ¹⁸ O	557	Wilson (1999)
¹⁶ O/ ¹⁷ O	2005	Wilson (1999)

Table 2. ISM values of isotopic ratios assumed in this work

show the line peak ratio for the ¹²CO and C¹⁸O¹⁶O Q branches, assuming ¹²CO/C¹⁸O¹⁶O = 278.5 (which is half the ISM *atomic* ratio of 557; Wilson 1999, since there are two O's in CO₂). The observed value of 2.97 ± 0.36 is also consistent with $N_{\text{CO}_2} \gtrsim 10^{18} \text{ cm}^{-2}$. The column density and the molecular ratio are degenerate, however; lower ¹²CO₂/¹³CO₂ or ¹²CO/C¹⁸O¹⁶O ratios would imply a lower best-fit column density.

Given the degeneracies inherent in this modeling, we therefore cannot independently fit the column density and abundance ratio. Instead, we test whether the ISM abundance ratios can provide a good fit to the data, and investigate the implications of the results. We start by fixing the C ratios to the ISM value (¹²C/¹³C=68), fitting both the ¹²CO₂ and ¹³CO₂ Q branches, and using the resulting constraints to pinpoint the oxygen isotope ratios. The χ^2 diagram in Figure 9(a) shows that using ¹³CO₂ along with ¹²CO₂ in the fit moves the best-fit model towards higher N_{CO₂} values (consistent with Figure 7(b)) and lower T values. The best-fit model has N_{CO₂} = $3.5 \times 10^{18} \text{ cm}^{-2}$, T = 325 K and R = 0.58 AU. A degeneracy is still present due to the ¹²CO₂

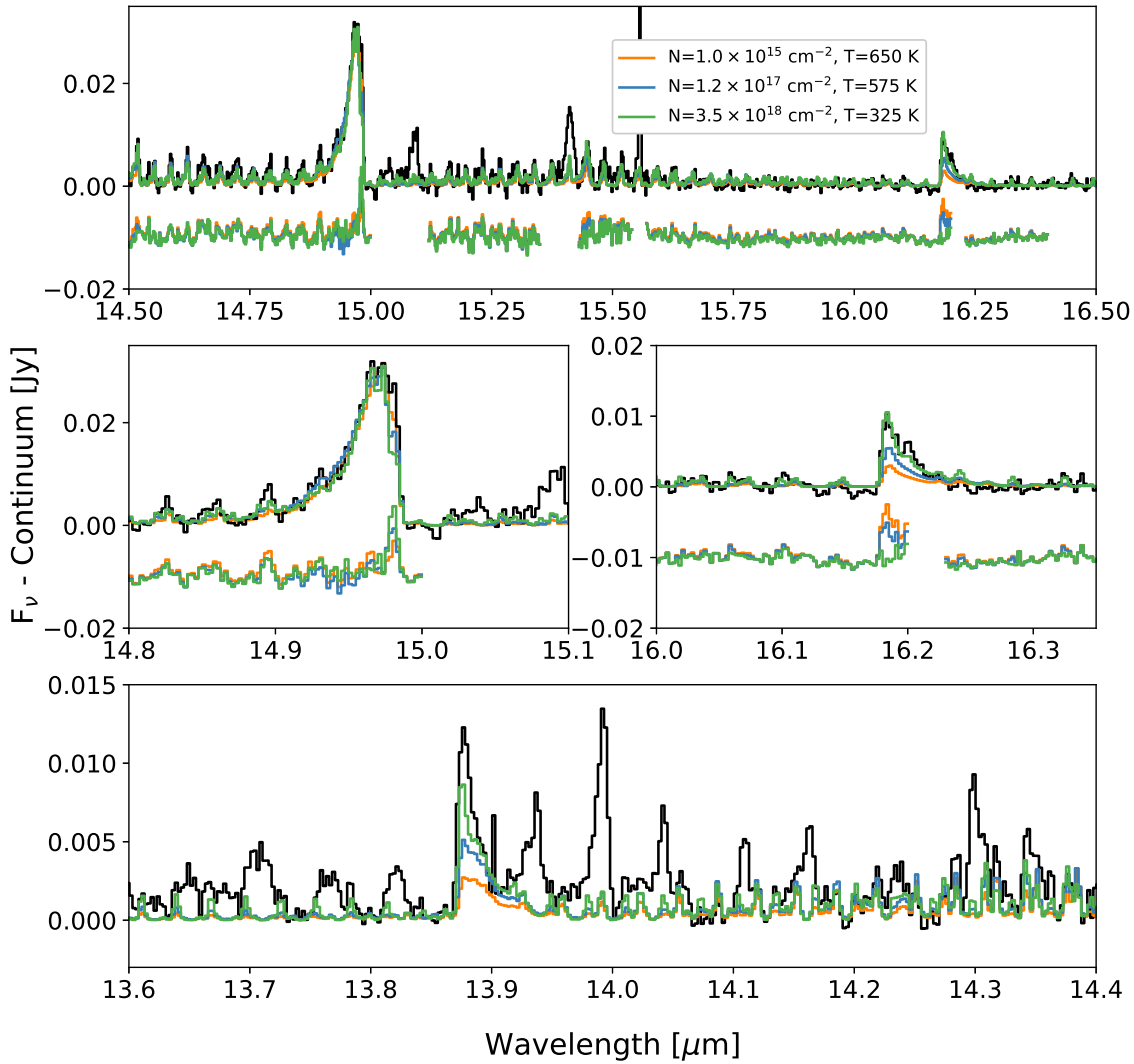


Figure 8. Continuum and water-subtracted MIRI-MRS spectrum of MY Lup (black) compared with 3 slab models (colors). Residuals (with regions contaminated by isotopologue or atomic emission removed) are shown below. The middle panels highlight two regions with significant differences between the residuals. The bottom panel highlights a CO₂ feature in the HCN-emitting region, which was not included in the calculation of χ^2 .

issues highlighted in Figure 8, but Figure 9(b) shows that the ¹³CO₂ Q branch is very sensitive to N_{CO_2} .

Using the best-fit N_{CO_2} and T, we then vary the oxygen isotope ratios to find those most consistent with the data. We find a best-fit ¹⁶O/¹⁸O ratio of 381^{+132}_{-100} ; the best fit and $\pm 1\sigma$ models are shown in Figure 9(c). The C¹⁷O¹⁶O feature is consistent with a best-fit ¹⁶O/¹⁷O ratio of 2272_{-882} , but higher ratios are also consistent with this marginal detection. The best fit model and -1σ model are shown in Figure 9(d).

Alternatively, we can fix the ¹⁶O/¹⁸O to the ISM value of 557 (Wilson 1999), and explore the implications of this as-

sumption. Figure 10(a) shows a χ^2 diagram for a fit to the combined C¹⁸O¹⁶O and CO₂ spectrum. The best-fit model parameters are: $N_{\text{CO}_2} = 5.6 \times 10^{18} \text{ cm}^{-2}$, T= 300 K and R= 0.65 AU. A degeneracy between N and T remains in the χ^2 analysis, but Figure 10(b) shows that that the C¹⁸O¹⁶O Q-branch feature is quite sensitive to the CO₂ column density. With T and N_{CO_2} fixed to these best-fit values, we find a best-fit ¹²CO₂/¹³CO₂ ratio of 77^{+84}_{-25} and a best-fit ¹⁶O/¹⁷O ratio $>3109_{-1028}$. These fits are shown in Figure 10(c) and (d).

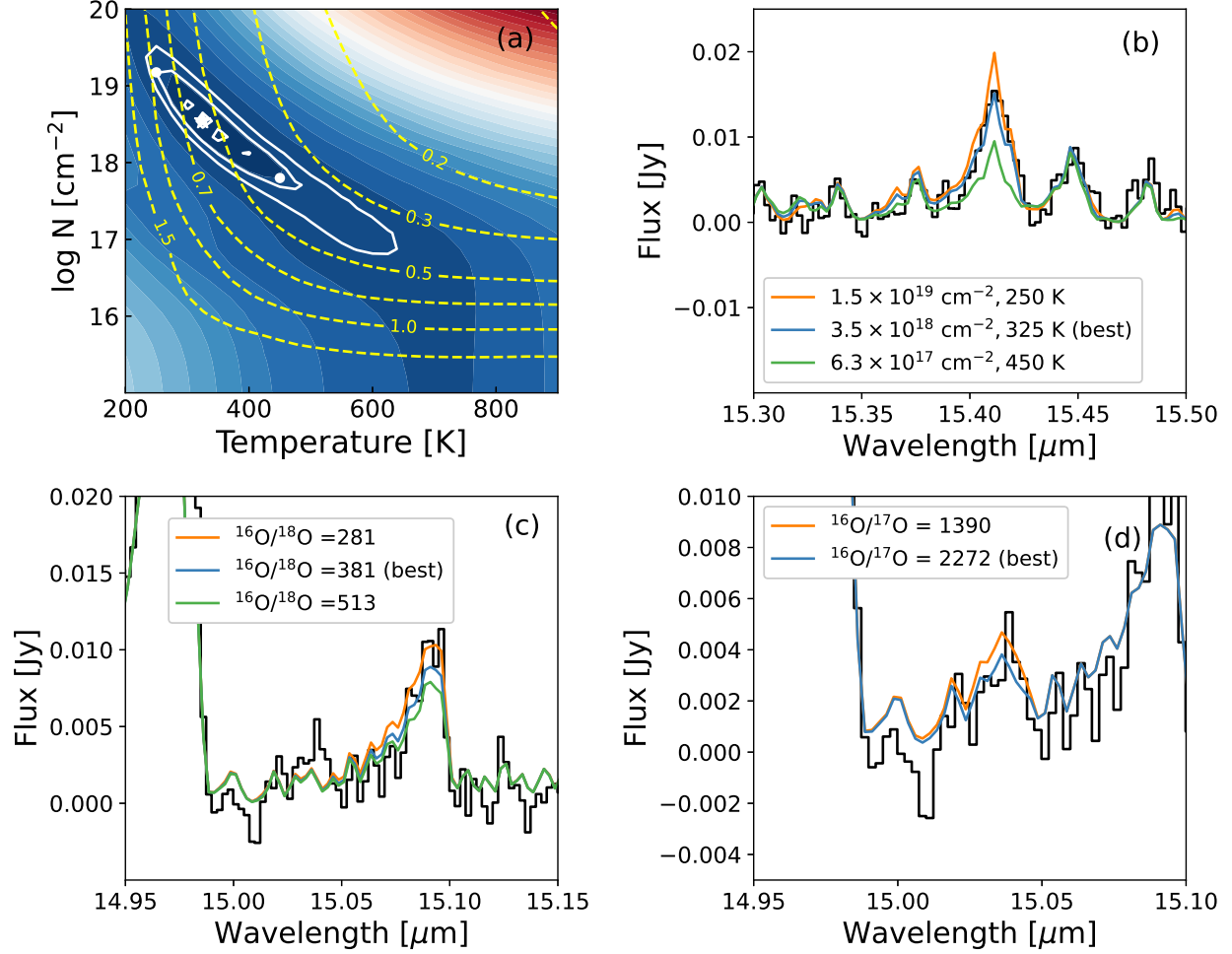


Figure 9. Analysis with C ratios fixed to ISM values. (a) χ^2 diagram for combined $^{13}\text{CO}_2$ and $^{12}\text{CO}_2$ fit. White star shows the best-fit model, while white circles show models highlighted in panel (b). White solid and yellow dashed lines have the same meaning as in Figure 7(a). (b) $^{13}\text{CO}_2$ Q branch overplotted with the best-fit model and two additional models at the edges of the 2σ χ^2 contour. Legend labels show the values of N_{CO_2} and T for these models. (c) $\text{C}^{18}\text{O}^{16}\text{O}$ Q branch overplotted with models assuming the best-fit $^{16}\text{O}/^{18}\text{O}$ ratio and those representing the best fit $\pm 1\sigma$. (d) $\text{C}^{17}\text{O}^{16}\text{O}$ Q branch overplotted with a model with the best-fit $^{16}\text{O}/^{17}\text{O}$ as well as one representing the best fit -1σ .

The results of both approaches are summarized in Table 1. Fits with either fixed C or fixed O isotope ratios produce similar best-fit model parameters, with $T = 300 - 325$ K, $N_{\text{CO}_2} = 3.5 - 5.6 \times 10^{18} \text{ cm}^{-2}$ and $R = 0.58 - 0.65$ AU.

4.3. Hydrogen Cyanide

In order to investigate HCN emission features in MY Lup’s spectrum, we first subtract both the best-fit water models and CO_2 models from the data. The CO_2 subtraction process is shown in Figure 11, demonstrating the substantial contribution from CO_2 at $\sim 13.9 \mu\text{m}$. The remainder of the HCN analysis utilizes the water and CO_2 -subtracted spectrum.

Figure 12 shows the HCN-emitting region, which demonstrates evidence for both HCN and H^{13}CN emission. We also note an emission feature located near the HC^{15}N Q branch at $\sim 14.06 \mu\text{m}$; given its tentative nature, we do not model this feature further. A fit to the HCN emission alone (excluding the region near the H^{13}CN feature) is performed using the

same procedure as for CO_2 ; in short, we iterate through a grid of N and T to create a model using “slabspec”, adjust the emitting area to best match the data, and compute χ^2 for each model. Figure 12(a) shows the resulting χ^2 diagram, which demonstrates a degeneracy between N and T. In panel (c), we highlight three models within the 1σ contour — the best-fit model, marked by a white star in panel (a), as well as two models marked by white circles. We additionally add emission from H^{13}CN assuming the same T and R as for HCN, but varying $N_{\text{H}^{13}\text{CN}}$ (and therefore, the $^{12}\text{C}/^{13}\text{C}$ ratio) to minimize the residuals. We can see that these three models produce subtle variations in the resulting spectrum, and no model is clearly preferred. Therefore, as with CO_2 , the C isotope ratio cannot be tightly constrained with these data.

If we instead fix $^{12}\text{C}/^{13}\text{C}$ to the ISM ratio of 68, and simultaneously fit both the HCN and H^{13}CN spectral regions, assuming they arise from a reservoir with the same N, T and R, the model parameters become more tightly constrained.

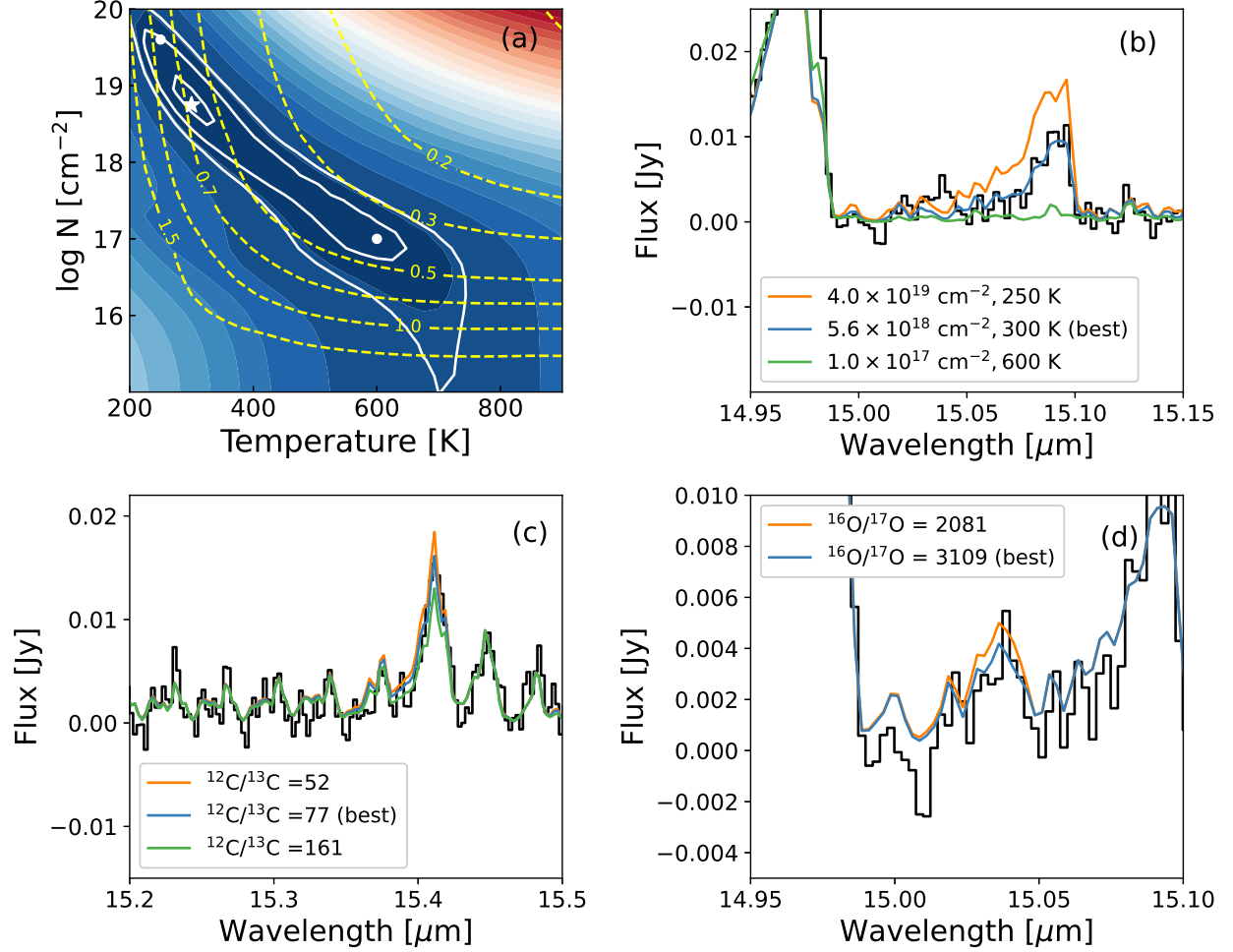


Figure 10. Analysis with $^{16}\text{O}/^{18}\text{O}$ ratio fixed to the ISM value. (a) χ^2 diagram for combined $\text{C}^{18}\text{O}^{16}\text{O}$ and CO_2 fit. The white star shows the best-fit model, while white circles show models highlighted in panel (b). White solid and yellow dashed lines have the same meaning as in Figure 9(a). (b) $\text{C}^{18}\text{O}^{16}\text{O}$ Q branch overplotted with the best-fit model and two additional models at the edges of the 2σ χ^2 contour. Legend labels show the values of N_{CO_2} and T for these models. (c) $^{13}\text{CO}_2$ Q branch overplotted with models assuming the best-fit $^{13}\text{CO}_2$ ratio and those representing the best fit $\pm 1\sigma$. (d) $\text{C}^{17}\text{O}^{16}\text{O}$ Q branch overplotted with a model with the best-fit $^{16}\text{O}/^{17}\text{O}$ as well as one representing the best fit -1σ .

The χ^2 contours are shown in Figure 12(b); the best-fit model has $N_{\text{HCN}} = 1.4 \times 10^{19} \text{ cm}^{-2}$, $N_{\text{H}^{13}\text{CN}} = 2.0 \times 10^{17} \text{ cm}^{-2}$, $T = 250 \text{ K}$ and $R = 0.61 \text{ AU}$. The best-fit model is also shown in Figure 12(d).

The model residuals show a potential feature near the C_2H_2 Q branch at $\sim 13.7 \mu\text{m}$. If we assume the C_2H_2 originates in a reservoir with the same emitting area and temperature as for the combined HCN and H^{13}CN fit, we find that $N_{\text{C}_2\text{H}_2} \lesssim 10^{16} \text{ cm}^{-2}$, implying $N_{\text{C}_2\text{H}_2}/N_{\text{HCN}} \lesssim 10^{-3}$.

5. DISCUSSION

5.1. Constraints on isotopic ratios

The discovery of multiple isotopologues of CO_2 emitted by the MY Lup disk opens the possibility of studying isotopic fractionation in inner disk atmospheres. In the context of isotope-selective photodissociation, the isotopic fractionation of a given molecule depends on whether the molecule

is produced in a region affected by CO self-shielding, and also whether the molecule is produced via a chemical pathway that includes the isotopically heavy water, or isotopically light CO. Calahan et al. (2022) suggest that the disk atmosphere probed by JWST is partially affected by CO self-shielding, and that observed water may appear enhanced in ^{18}O by a factor of ~ 2 relative to ISM values. But what about for CO_2 ? Bosman et al. (2022) suggest that the observed CO_2 arises from a similar disk atmospheric layer as does the water, which would lead to a prediction that observed CO_2 should also be isotopically heavy.

In Table 1, we compute the measured enhancements in heavy isotopes relative to the ISM value: R_i/R_{ISM} , where $R_i/R_{\text{ISM}} > 1$ implies enhancement of the heavy isotope relative to ISM values. While CO_2 shows potential enhancement by a factor of 1.5 in ^{18}O for our fixed-C ratio model sets, ^{17}O is depleted in those same models. It is not clear that there is

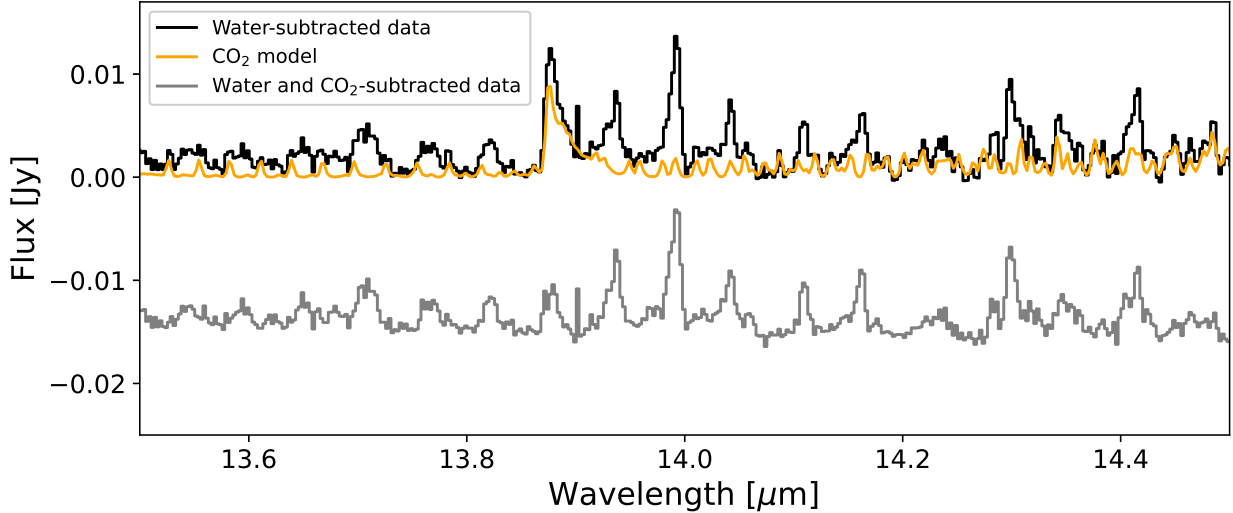


Figure 11. Subtraction of CO₂ model from water model-subtracted data in HCN-emitting region.

a mechanism to explain enhancement in one heavy isotope with simultaneous depletion in another. Isotopic ratios are also consistent with ISM values to within $\sim 2\sigma$, so observed enhancements and depletions may simply reflect our uncertainties at this time.

In Figure 13, we visually compare our derived oxygen isotope ratios from the CO₂ emission with the local ISM value, as well as with mass-dependent and mass-independent fractionation lines. We also show ratios measured via CO absorption associated with young stellar objects (Smith et al. 2015). As in Table 1, the ratios shown here are plotted relative to the ISM ratio, such that a positive δ means an enhancement in the rarer heavy isotope. We remind the reader that we derive our values from two different analysis approaches – fixed C and fixed O, as described in Section 4.2 — and that therefore, one of the points we show was artificially fixed to the ISM value on the x axis. We see visually that ¹⁷O is depleted according to both modeling approaches, while ¹⁸O is enhanced, although values are consistent with ISM values within the error bars.

Figure 13 also shows the carbon isotope ratio derived from the CO₂ emission, assuming a fixed Oxygen ratio, as compared to the ISM, the solar system, and the young stellar objects in Smith et al. (2015). The carbon isotope ratio is consistent with both the ISM and solar system values, as well as some of the sources from Smith et al. (2015).

Error bars on the isotope ratios remain too large to distinguish between different fractionation scenarios, and differences in the fixed-C and fixed-O analyses suggest a similar-sized systematic error. Therefore, additional error bar refinement would be helpful to make meaningful scientific conclusion about fractionation in inner disks. In addition, our analyses all assume that the isotopologues emit from the same reservoir. Given the complex vertical and radial temperature and density structures of protoplanetary disks, this assumption is certainly not strictly true. Nevertheless, the detection of multiple isotopologues in this source suggests a promis-

ing avenue for future work. Observations at higher spectral resolution could test the validity of the single reservoir assumption, and be used to better constrain emission models, although the CO₂ Q branches are not accessible from the ground. As we discuss in the next section, there are also several additional disks with high reported CO₂ column densities that would be worthy of follow-up study.

5.2. MY Lup’s unique spectrum

Amongst ~ 15 published MIRI-MRS protoplanetary disk spectra (see JDISCS and MINDS program descriptions in Pontoppidan et al. 2024 and Henning et al. 2024, respectively) and other spectra investigated thus far by the JDISCS team (34 disks total in programs 1549, 1640, 1584 and 2025; Arulanantham et al., 2025, in prep), MY Lup’s spectrum is the only to show emission from C¹⁸O¹⁶O. We consider here the possible causes for this unique detection.

Figure 14 shows a comparison of MY Lup’s best-fit slab model parameters with other published parameters for T Tauri disks (Gasman et al. 2023; Tabone et al. 2023; Schwarz et al. 2024; Banzatti et al. 2023; Xie et al. 2023; Grant et al. 2023; Pontoppidan et al. 2024; Muñoz-Romero et al. 2024). We note that these published spectra span a wide range of stellar mass, but no particular trend emerges related to that parameter. As discussed in Section 4.2 and shown in Figure 7, one should expect that the detection of CO₂ isotopologues would be prompted by high CO₂ column densities, as a high column density reduces the line peak ratio between the primary and secondary/tertiary isotopologues. MY Lup has a higher CO₂ column density than GW Lup, the latter of which had a reported detection of ¹³CO₂ (Grant et al. 2023). However, MY Lup has a lower reported CO₂ column density than Sz 98 and DF Tau. Gasman et al. (2023) report that the best-fit CO₂ column density for Sz 98 is uncertain, and also provide an alternative lower-*N* model, which we also show in Figure 14. We find that with an ISM ¹²C/¹³C ratio and the high-*N* model parameters given in Gasman et al. (2023),

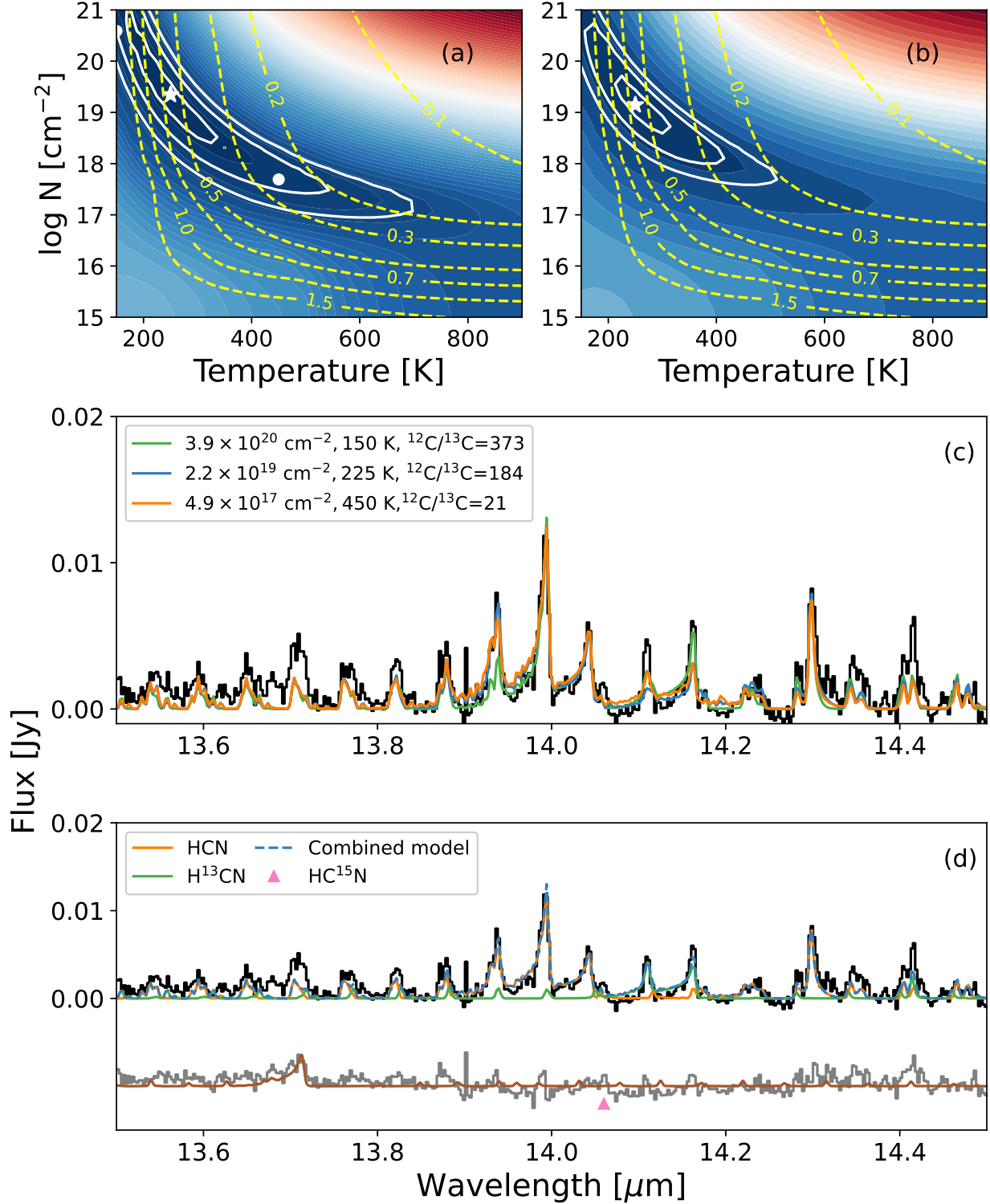


Figure 12. (a) χ^2 contours for a fit to HCN only. Here and in panel (b), a white star marks the best-fit model; white circles mark additional models explored in panel (c). White contours mark 1, 2 and 3 σ confidence intervals assuming the minimum $\chi^2_{\text{red}} = 1$. (b) χ^2 contours for a combined fit to HCN and H¹³CN, with $^{12}\text{C}/^{13}\text{C}$ fixed to the ISM ratio. (c) Three models (with parameters marked in panel (a)) with differing $^{12}\text{C}/^{13}\text{C}$ ratios, but only subtle changes in the quality of the model fit. (d) Best-fit model for HCN and H¹³CN combined ($N_{\text{HCN}} = 1.4 \times 10^{19} \text{ cm}^{-2}$, $N_{\text{H}^{13}\text{CN}} = 2.0 \times 10^{17} \text{ cm}^{-2}$, $T = 250 \text{ K}$ and $R = 0.61 \text{ AU}$), with $^{12}\text{C}/^{13}\text{C}$ fixed to the ISM ratio, corresponding to the star in panel (b). A pink triangle marks a tentative detection of HC¹⁵N, and the brown curve shows a C₂H₂ model with T= 250 K, R= 0.61 AU and N= 10¹⁶ cm⁻².

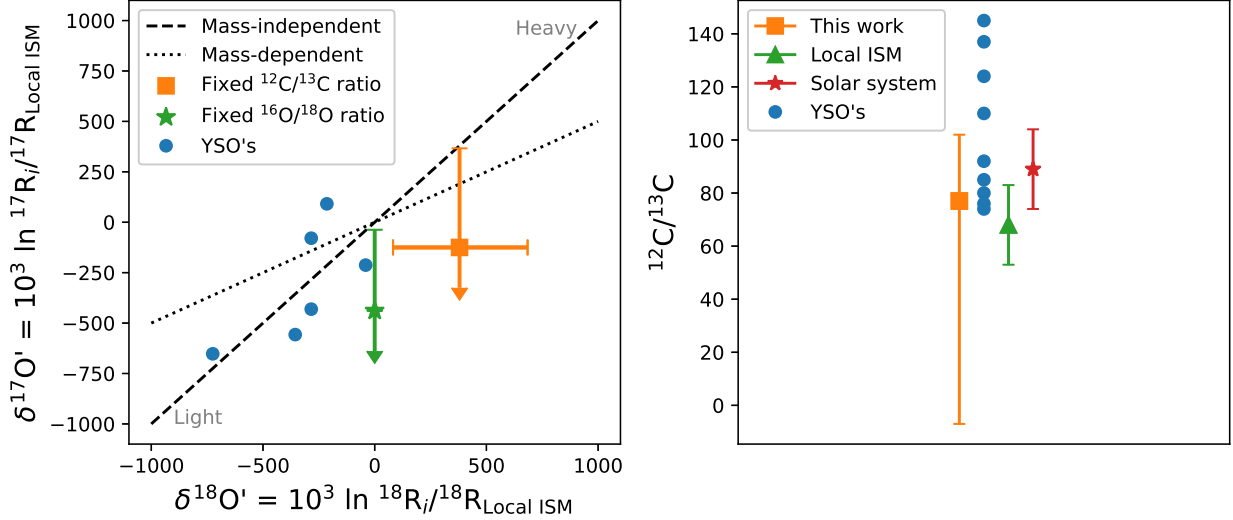


Figure 13. Left: Oxygen isotope fractionation relative to ISM ratios; following standard cosmochemistry notation, heavier O is on the upper right of the plot. $\delta^{17}\text{O}'$ is defined as $10^3 \ln (^{17}\text{R}_i/^{17}\text{R}_{\text{Local ISM}})$, $\delta^{18}\text{O}' = 10^3 \ln (^{18}\text{R}_i/^{18}\text{R}_{\text{Local ISM}})$, and R_i is the atomic ratio while $^{17}\text{R}_{\text{Local ISM}}$ and $^{18}\text{R}_{\text{Local ISM}}$ are the local ISM atomic ratios $^{18}\text{O}/^{16}\text{O}$ and $^{17}\text{O}/^{16}\text{O}$, i.e., the inverse of that used in the rest of the text — see also Table 1. Dotted and dashed lines have slope 0.5 and 1, as expected for mass-independent or mass-dependent fractionation, respectively. The green star and orange square mark our values derived from CO_2 emission from MY Lup, as described in Section 4.2. Right: Carbon isotope ratios derived from MY Lup’s CO_2 emission (assuming fixed Oxygen ratio, as described in Section 4.2), compared to values from Smith et al. (2015), the local ISM, and the solar system (Milam et al. 2005, and references therein). Points are offset on the x axis for clarity.

there should have been strong CO_2 isotopologue emission from Sz 98. Therefore, we suggest that either a lower N is required, or Carbon must be highly fractionated in the Sz 98 disk. DF Tau has a water-rich spectrum (Grant et al. 2024), which may have obscured the weaker CO_2 isotopologues. In Appendix C, we compare the spectrum of MY Lup with the spectra of Sz 98, GW Lup, and DF Tau.

The middle panel of Figure 14 also shows that the HCN column density and temperature are strikingly different for MY Lup as compared to other published disk spectra. And the right panel demonstrates that while the water emission from MY Lup is consistent with “cool” water temperatures in multi-component slab model fits, MY Lup is the only disk seemingly lacking a warm/hot water component.

The presence of CO_2 and HCN isotopologues in the MY Lup spectrum is likely due to their high overall column densities, but why are these column densities so high in the MY Lup disk? One distinguishing characteristic of MY Lup is its high (70–80°) inclination. As shown schematically in Figure 15, a high inclination can reveal a larger line-of-sight column of gas above the $\tau_{\text{dust}} = 1$ surface. For a plane-parallel slab, the path length scales as $\sec(i)$, resulting in a factor of 3–4 enhancement for MY Lup’s inclination, but any dust settling ratio would increase this enhancement level. Dust settling itself can also increase infrared molecular line/continuum ratios (Meijerink et al. 2009; Bosman et al. 2017), even with no inclination effect. These possibilities seem unlikely to fully explain MY Lup’s spectrum, however, as they should affect all molecular emission lines; however, MY Lup has weak water emission, only a marginal possible detection of C_2H_2 , and no detections of CO or additional molecules.

Inner disk clearing likely also plays an important role in producing MY Lup’s spectrum. Although prior work has been ambivalent about the extent of clearing in MY Lup’s inner disk (Romero et al. 2012; van der Marel et al. 2018; Alcalá et al. 2019), the presence of photospheric features in the $5\mu\text{m}$ region of the MRS spectrum confirms a low degree of veiling (see Figure 2). Lower veiling at $\sim 5\mu\text{m}$ is consistent with reduced emission from small dust grains in the inner disk (Salyk et al. 2009), as for so-called “transition” disks (Koerner et al. 1993; Calvet et al. 2002). Also, MY Lup’s molecular emission is consistent with colder temperatures as compared with other observed disks, particularly for HCN and H_2O (see Figure 14). As modeled by Vlasblom et al. (2024) in an effort to explain the strong CO_2 emission from GW Lup’s disk (Grant et al. 2023), if the inner clearing extends to between the water and CO_2 snowlines, it may greatly reduce the water/ CO_2 line ratios.

Bosman et al. (2017) also suggest that inward drift of CO_2 ice-covered pebbles could enhance inner disk CO_2 column densities, and predict that a cold excitation temperature would be observed for such emission. Pebble drift in general would be expected to also enhance water vapor emission (Kalyaan et al. 2021, Houge et al. 2024, in preparation), inconsistent with MY Lup’s spectrum, but inner disk clearing may act to dissociate the liberated water vapor (Bethell & Bergin 2009).

It should be highlighted that although emitting areas from LTE modeling are often converted to disk radii, the conversion $R = \sqrt{A/\pi \cos i}$ only holds for a full disk that approximates a circular geometry. In the case of a disk with a large

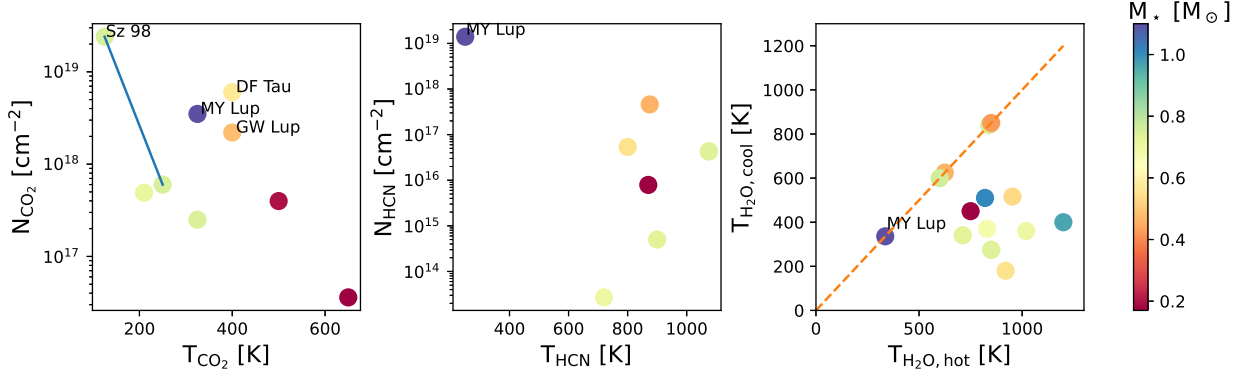


Figure 14. Left: Best-fit CO_2 column density vs. temperature for published slab models. For 2MASS-J16053215-1933159 we show the “Component II” fits, which are consistent with the non-detection of $^{13}\text{CO}_2$ in that source (Tabone et al. 2023), and for Sz 98 we show both reported models (Gasman et al. 2023) connected by a blue line. Sources with the three highest column densities are labeled. Center: Best-fit HCN column density vs. temperature. Right: Best-fit cold vs. hot water temperatures. Sources on the 1:1 line were fit with only a single water component. If more than two components were used in the fit, we show the warmest and coolest components. Slab model parameters shown in all three panels collected from Gasman et al. (2023); Tabone et al. (2023); Schwarz et al. (2024); Banzatti et al. (2023); Xie et al. (2023); Grant et al. (2023); Pontoppidan et al. (2024); Muñoz-Romero et al. (2024); Grant et al. (2024); Perotti et al. (2023); Temmink et al. (2024a,b). Color bar shows the stellar mass in solar masses.

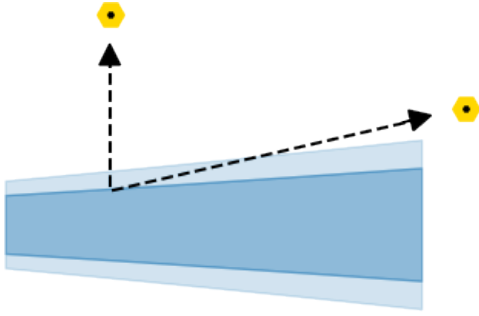


Figure 15. Schematic demonstrating how an edge-on line of sight can increase the optical path through the disk atmosphere as compared to a face-on line of sight.

inner clearing, the derived R reflects the width of the emitting ring of material, but not its physical location in the disk. Thus, we cannot say whether the CO_2 and/or water may arise from beyond a cleared inner region. The high inclination of MY Lup’s disk could also produce self-absorption in the molecular lines, which would affect measured emitted fluxes. Kinematic information from spectrally-resolved line shapes could provide us with the physical location of the emission, and indicate the presence of any self-absorption.

The high column and low temperature of HCN (as well as the correspondingly high HCN/ H_2O column density ratio of 14) are also unusual in MY Lup’s spectrum (see Figure 14). While high C/O ratios could enhance HCN abundances in the disk atmosphere, high C/O would be expected to enhance C_2H_2 abundances to an even greater degree (Najita et

al. 2011), which we do not observe. In addition, given the similar adsorption energies for H_2O and HCN (Aikawa et al. 1997), one might therefore expect the inner clearing proposed by Vlasblom et al. (2024) and Grant et al. (2023) to also suppress HCN. Therefore, explaining MY Lup’s spectrum may require some unique chemistry that has yet to be fully explained.

All abundances in this work do assume LTE excitation, and this assumption can influence derived column densities. For HCN, the key observational signature driving the slab model fits to high N and low T is a low relative peak ratio of the HCN Q branches (for the primary isotopologue) coupled with low flux in the high rotational states (i.e., the Q branches appear skinny, rather than fat). Therefore, the signature driving our model fits to low T and high N could potentially be mimicked if the vibrational states can be populated non-thermally, even while the gas temperature remains low. Non-LTE excitation has previously been predicted for MIRI-MRS HCN lines (Bruderer et al. 2015). However, the models of Bruderer et al. (2015) have neither successfully matched resolved HCN lineshapes nor the strength of vibrationally excited states (Najita et al. 2018). Since the rotational and vibrational states can be successfully fit with a single slab model, it is not obvious that non-LTE excitation is required to explain MY Lup’s HCN spectrum. The high HCN column density is also supported by the isotopologue detection.

6. CONCLUSIONS

In conclusion, we report strong CO_2 and HCN emission, including from isotopologues of both molecules, but weak water emission from the protoplanetary disk around the T Tauri star MY Lup. Slab modeling suggests relatively high column densities of CO_2 and HCN, but a typical column density of water. Isotopologue detections are helpful in con-

straining column densities in otherwise degenerate modeling, although this requires the fixing of isotopologue ratios. The temperatures of all molecules are cold compared to most other disks, particularly for HCN and water.

Using the isotopologue detections, we investigate whether there is any evidence for isotopic fractionation. Systematic errors and modeling assumptions limit interpretations, although the observations are consistent with ISM isotope ratios to within the error bars. However, the detection of isotopologues in this source makes it an ideal target for follow-up observations, ideally with high resolution spectrographs. High resolution spectra would have higher molecular line/continuum ratios, enhancing the detectability of the isotopologue signatures, and provide kinematic information to reduce modeling degeneracies. Other protoplanetary disks with high molecular column densities would also be promising targets for such follow-up work.

Given its cold molecular temperatures, weak water emission, and high CO₂ and HCN column densities, MY Lup appears unique amongst protoplanetary disks observed with MIRI-MRS to date. We attribute this unique spectrum to a combination of inner disk clearing and a high disk inclination, although additional unusual chemical conditions may also be present.

This project was supported by the STScI grant JWST-GO-01584.001-A “A DSHARP-MIRI Treasury survey of Chemistry in Planet-forming Regions”. A portion of this research was carried out at the Jet Propulsion Laboratory, California Institute of Technology, under a contract with the National Aeronautics and Space Administration (80NM0018D0004). This research used the SpExoDisks Database at spexodisks.com.

APPENDIX

A. HI EMISSION AND ABSORPTION

Figure 16 shows a close up of H I transitions in the MY Lup spectrum. The H I spectrum shows a combination of emission and absorption features. Emission from several H I transitions has been calibrated as a tracer of disk accretion (e.g. Muzerolle et al. 1998), including H I (7-6), which appears in MIRI-MRS data (Rigliaco et al. 2015). The presence of H I absorption could indicate absorption by foreground material in the disk or wind of this edge-on disk, although it is unclear why only some lines are in absorption (in particular, the lines with lower level $n = 7$), while others are in emission. Absorption lines all appear at the shortest wavelengths, and in MRS Channel 1, where a standard star is used as a telluric calibrator, rather than the asteroid. However, we find no indication that the standard star is introducing spurious absorption. It may instead be the case that we observe the stellar H I absorption at shorter wavelengths, where veiling is lower, and accretion-produced H I emission at longer wavelengths, where veiling is higher and fills in the photospheric absorption. In-depth analysis of the H I transitions is left as future work.

B. EVIDENCE FOR NON-LTE EXCITATION OF CO₂

Figure 17 shows upper level energies for the two emitting regions highlighted in Section 4.2 and Figure 8. Labels are the quantum numbers associated with the upper level (v_1, v_2, l_2, v_3, r , where v_i are i th vibrational levels, l_2 is the angular momentum of the v_2 state, and r is the Fermi resonance symmetry), as obtained from HITRAN (Gordon et al. 2022) and described in Rothman et al. (2005). Dashed vertical lines highlight the regions where residuals distinguish between preferred models.

The left- and right-hand plots highlight two features that require high column densities to match the observed spectrum. The 13.88 μm feature is produced by a transition from 10001 to 01101, while the 16.2 μm feature is produced by a transition from the 10002 to the 01101 state. Thus, both represent transitions between $v_1 = 1$ and $v_2 = 1$ states.

The middle plot is the primary CO₂ Q branch feature, and the shape of the “red edge” highlighted with the dashed vertical lines depends on the relative strength of the fundamental ($v_2=1$) vs. hot-band ($v_2 \geq 2$) lines. In the context of the LTE models, low column densities are required to fit the observed “red edge”; higher column densities create more emission in the excited states, producing a sharper dropoff on the “red edge” of the Q branch than is observed in the data. Since this feature depends on the states with $v_2 \geq 2$, its shape may be more affected by non-LTE excitation.

C. COMPARISON WITH OTHER CO₂-RICH DISKS

Figure 18 shows a comparison of the CO₂-emitting region for the four disks with the highest reported CO₂ column densities. Locations of the isotopologue Q branches are highlighted in the middle panel. The left and right panels show other regions with CO₂ emission features consistent with high N_{CO₂} (see Figure 8 and associated discussion).

REFERENCES

- Aikawa, Y., Umebayashi, T., Nakano, T., et al. 1997, ApJL, 486, L51. doi:10.1086/310837
- Alcalá, J. M., Manara, C. F., Natta, A., et al. 2017, A&A, 600, A20. doi:10.1051/0004-6361/201629929
- Alcalá, J. M., Manara, C. F., France, K., et al. 2019, A&A, 629, A108. doi:10.1051/0004-6361/201935657
- Andrews, S. M., Huang, J., Pérez, L. M., et al. 2018, ApJL, 869, L41. doi:10.3847/2041-8213/aaf741
- Avenhaus, H., Quanz, S. P., Garufi, A., et al. 2018, ApJ, 863, 44. doi:10.3847/1538-4357/aab846
- Banzatti, A., Pontoppidan, K. M., Carr, J. S., et al. 2023, ApJL, 957, L22. doi:10.3847/2041-8213/acf5ec
- Banzatti, A., Salyk, C., Pontoppidan, K. M., et al. 2024, arXiv:2409.16255. doi:10.48550/arXiv.2409.16255
- Bergin, E. A., Bosman, A., Teague, R., et al. 2024, ApJ, 965, 147. doi:10.3847/1538-4357/ad3443
- Bethell, T. & Bergin, E. 2009, Science, 326, 1675. doi:10.1126/science.1176879
- Bockelée-Morvan, D., Calmonte, U., Charnley, S., et al. 2015, SSRv, 197, 47. doi:10.1007/s11214-015-0156-9
- Bosman, A. D., Bruderer, S., & van Dishoeck, E. F. 2017, A&A, 601, A36. doi:10.1051/0004-6361/201629946
- Bosman, A. D., Bergin, E. A., Calahan, J. K., et al. 2022, ApJL, 933, L40. doi:10.3847/2041-8213/ac7d9f
- Bredall, J. W., Shappee, B. J., Gaidos, E., et al. 2020, MNRAS, 496, 3257. doi:10.1093/mnras/staa1588
- Bruderer, S., Harsono, D., & van Dishoeck, E. F. 2015, A&A, 575, A94. doi:10.1051/0004-6361/201425009
- Bushouse, H., Eisenhamer, J., Dencheva, N., et al. 2024, Zenodo
- Calahan, J. K., Bergin, E. A., & Bosman, A. D. 2022, ApJL, 934, L14. doi:10.3847/2041-8213/ac7e55

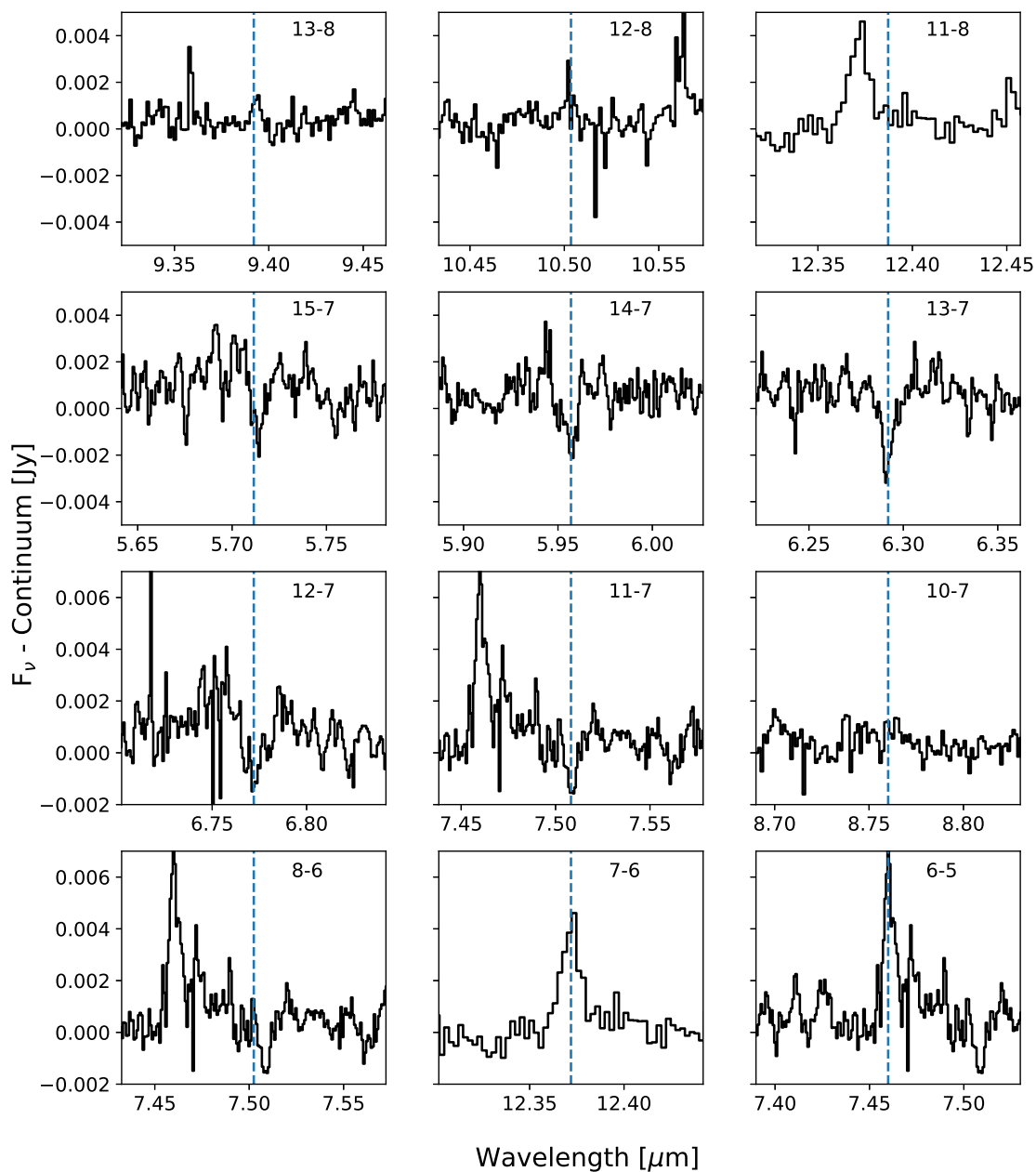


Figure 16. Close-up of selected HI transitions. Upper and lower electronic levels are shown in the upper right of each panel.

Calvet, N., D’Alessio, P., Hartmann, L., et al. 2002, *ApJ*, 568,
1008. doi:10.1086/339061

Carr, J. S. & Najita, J. R. 2008, *Science*, 319, 1504.
doi:10.1126/science.1153807

Carr, J. S. & Najita, J. R. 2011, *ApJ*, 733, 102.
doi:10.1088/0004-637X/733/2/102

Clayton, R. N., Grossman, L., & Mayeda, T. K. 1973, *Science*,
182, 485. doi:10.1126/science.182.4111.485

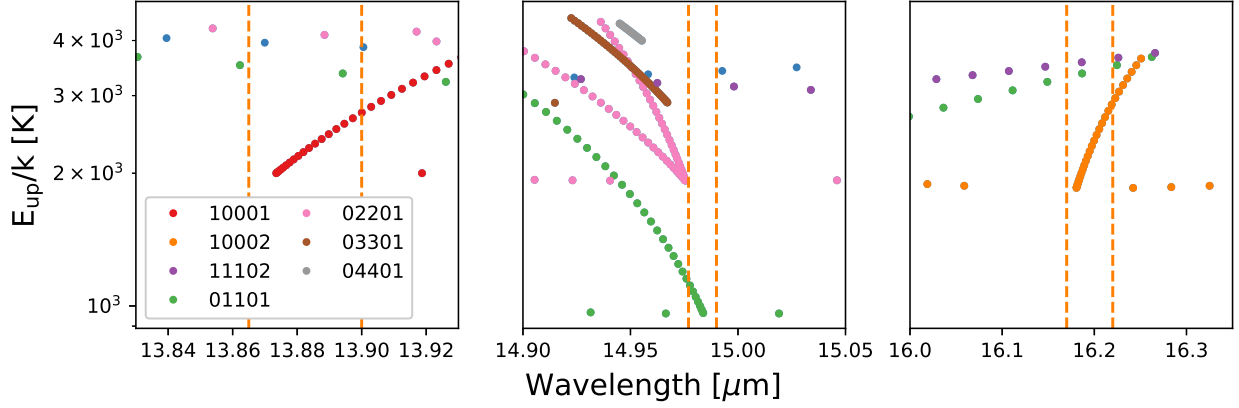


Figure 17. Upper level energies of emission lines in regions highlighted in Section 4.2 (from HITRAN database; Gordon et al. 2022); labels show the upper state quantum numbers (v_1, v_2, l_2, v_3, r) where v_i are i th vibrational levels, l_2 is the angular momentum of the v_2 state, and r is the Fermi resonance symmetry. Dashed vertical lines mark regions with large modeling residuals discussed in the text.

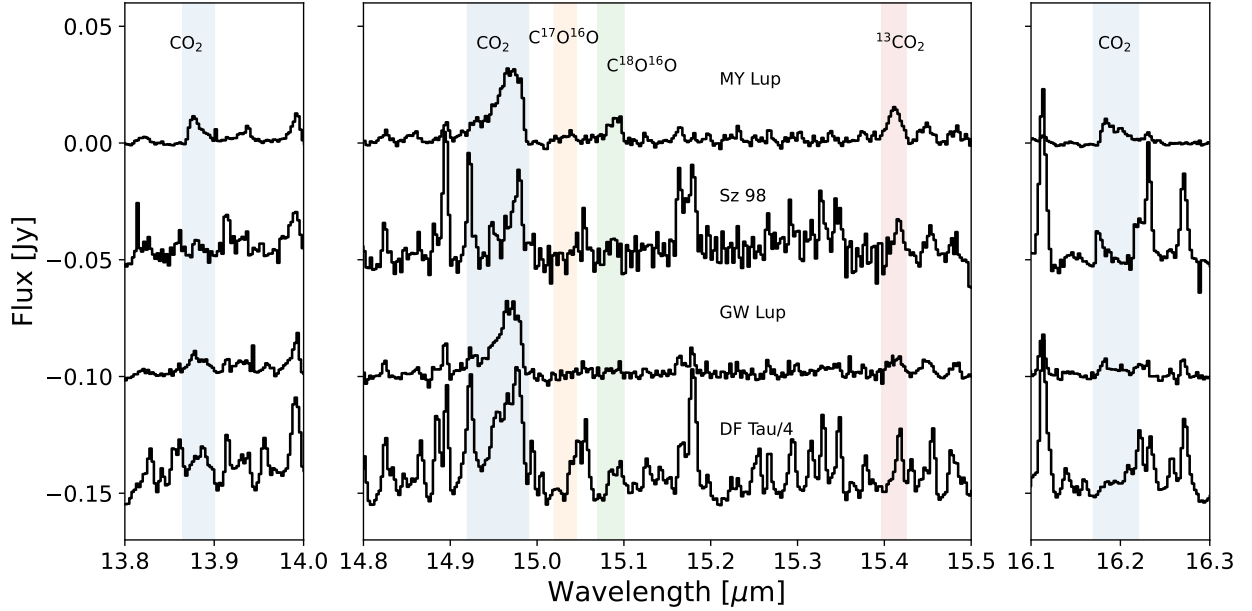


Figure 18. Continuum-subtracted MIRI-MRS spectra (reduced by the JDISCS team Pontoppidan et al. 2024) for the four sources with the highest reported CO_2 column densities: MY Lup (this work), Sz 98 (Gasman et al. 2023), GW Lup (Grant et al. 2023) and DF Tau (Grant et al. 2024). The DF Tau line spectrum has been divided by four for clarity. Colored bars in the central panel mark the locations of the primary Q branches of CO_2 and its isotopologues. The left and right panels show other regions with CO_2 emission features consistent with high N_{CO_2}

Foreman-Mackey, D., Hogg, D. W., Lang, D., et al. 2013, *PASP*, 125, 306. doi:10.1086/670067

Gasman, D., van Dishoeck, E. F., Grant, S. L., et al. 2023, *A&A*, 679, A117. doi:10.1051/0004-6361/202347005

Gordon, I. E., Rothman, L. S., Hargreaves, R. J., et al. 2022, *JQSRT*, 277, 107949. doi:10.1016/j.jqsrt.2021.107949

Grant, S. L., van Dishoeck, E. F., Tabone, B., et al. 2023, *ApJL*, 947, L6. doi:10.3847/2041-8213/acc44b

Grant, S. L., Kurtovic, N. T., van Dishoeck, E. F., et al. 2024, arXiv:2406.10217. doi:10.48550/arXiv.2406.10217

Henning, T., Kamp, I., Samland, M., et al. 2024, *PASP*, 136, 054302. doi:10.1088/1538-3873/ad3455

Hily-Blant, P., Magalhaes, V., Kastner, J., et al. 2017, *A&A*, 603, L6. doi:10.1051/0004-6361/201730524

Hily-Blant, P., Magalhaes de Souza, V., Kastner, J., et al. 2019, *A&A*, 632, L12. doi:10.1051/0004-6361/201936750

Houck, J. R., Roellig, T. L., van Cleve, J., et al. 2004, *ApJS*, 154, 18. doi:10.1086/423134

Huang, J., Andrews, S. M., Dullemond, C. P., et al. 2018, *ApJL*, 869, L42. doi:10.3847/2041-8213/aaf740

- Kalyaan, A., Pinilla, P., Krijt, S., et al. 2021, *ApJ*, 921, 84.
doi:10.3847/1538-4357/ac1e96
- Karhu, J.A., Bekker, A. (2023). Carbon Isotopes in the Solar System. In: Gargaud, M., et al. *Encyclopedia of Astrobiology*. Springer, Berlin, Heidelberg.
https://doi.org/10.1007/978-3-662-65093-6_5395
- Koerner, D. W., Sargent, A. I., & Beckwith, S. V. W. 1993, *Icarus*, 106, 2. doi:10.1006/icar.1993.1154
- Lis, D. C., Biver, N., Bockelée-Morvan, D., et al. 2013, *ApJL*, 774, L3. doi:10.1088/2041-8205/774/1/L3
- Long, F., Pascucci, I., Houge, A., et al. 2025, *ApJL*, 978, L30. doi:10.3847/2041-8213/ad99d2
- Lyons, J. R. & Young, E. D. 2005, *Nature*, 435, 317. doi:10.1038/nature03557
- Marty, B. 2012, *Earth and Planetary Science Letters*, 313, 56. doi:10.1016/j.epsl.2011.10.040
- McKeegan, K. D., Kallio, A. P. A., Heber, V. S., et al. 2011, *Science*, 332, 1528. doi:10.1126/science.1204636
- Meijerink, R., Pontoppidan, K. M., Blake, G. A., et al. 2009, *ApJ*, 704, 1471. doi:10.1088/0004-637X/704/2/1471
- Milam, S. N., Savage, C., Brewster, M. A., et al. 2005, *ApJ*, 634, 1126. doi:10.1086/497123
- Miotello, A., Bruderer, S., & van Dishoeck, E. F. 2014, *A&A*, 572, A96. doi:10.1051/0004-6361/201424712
- Moynier, F., Dauphas, N., & Podosek, F. A. 2009, *ApJL*, 700, L92. doi:10.1088/0004-637X/700/2/L92
- Muñoz-Romero, C. E., Öberg, K. I., Banzatti, A., et al. 2024, *ApJ*, 964, 36. doi:10.3847/1538-4357/ad20e9
- Muzerolle, J., Hartmann, L., & Calvet, N. 1998, *AJ*, 116, 2965. doi:10.1086/300636
- Najita, J. R., Ádámkóvics, M., & Glassgold, A. E. 2011, *ApJ*, 743, 147. doi:10.1088/0004-637X/743/2/147
- Najita, J. R., Carr, J. S., Salyk, C., et al. 2018, *ApJ*, 862, 122. doi:10.3847/1538-4357/aaca39
- Perotti, G., Christiaens, V., Henning, T., et al. 2023, *Nature*, 620, 516. doi:10.1038/s41586-023-06317-9
- Pontoppidan, K. M., Salyk, C., Blake, G. A., et al. 2010, *ApJ*, 720, 887. doi:10.1088/0004-637X/720/1/887
- Pontoppidan, K. M., Salyk, C., Banzatti, A., et al. 2024, *ApJ*, 963, 158. doi:10.3847/1538-4357/ad20f0
- Pringle, E. A., Savage, P. S., Jackson, M. G., et al. 2013, *ApJ*, 779, 123. doi:10.1088/0004-637X/779/2/123
- Rieke, G. H., Wright, G. S., Böker, T., et al. 2015, *PASP*, 127, 584. doi:10.1086/682252
- Rigliaco, E., Pascucci, I., Duchene, G., et al. 2015, *ApJ*, 801, 31. doi:10.1088/0004-637X/801/1/31
- Romero, G. A., Schreiber, M. R., Cieza, L. A., et al. 2012, *ApJ*, 749, 79. doi:10.1088/0004-637X/749/1/79
- Rothman, L. S., Jacquemart, D., Barbe, A., et al. 2005, *JQSRT*, 96, 139. doi:10.1016/j.jqsrt.2004.10.008
- Salyk, C., Pontoppidan, K. M., Blake, G. A., et al. 2008, *ApJL*, 676, L49. doi:10.1086/586894
- Salyk, C., Blake, G. A., Boogert, A. C. A., et al. 2009, *ApJ*, 699, 330. doi:10.1088/0004-637X/699/1/330
- github.com/csalyk/spectools_ir: First release, v1.0.0, Zenodo, 1104
doi: 10.5281/zenodo.5818682
- Savitzky, A. & Golay, M. J. E. 1964, *Analytical Chemistry*, 36, 1627
- Schwarz, K. R., Henning, T., Christiaens, V., et al. 2024, *ApJ*, 962, 8. doi:10.3847/1538-4357/ad1393
- Smith, R. L., Pontoppidan, K. M., Young, E. D., et al. 2009, *ApJ*, 701, 163. doi:10.1088/0004-637X/701/1/163
- Smith, R. L., Pontoppidan, K. M., Young, E. D., et al. 2015, *ApJ*, 813, 120. doi:10.1088/0004-637X/813/2/120
- Tabone, B., Bettoni, G., van Dishoeck, E. F., et al. 2023, *Nature Astronomy*, 7, 805. doi:10.1038/s41550-023-01965-3
- Tashkun, S. A., Perevalov, V. I., Teffo, J.-L., et al. 2003, *JQSRT*, 82, 165. doi:10.1016/S0022-4073(03)00152-3
- Temmink, M., van Dishoeck, E. F., Grant, S. L., et al. 2024, *A&A*, 686, A117. doi:10.1051/0004-6361/202348911
- Temmink, M., van Dishoeck, E. F., Gasman, D., et al. 2024, *A&A*, 689, A330. doi:10.1051/0004-6361/202450355
- Thiemens, M. H. & Heidenreich, J. E. 1983, *Science*, 219, 1073. doi:10.1126/science.219.4588.1073
- van der Marel, N., Williams, J. P., Ansdell, M., et al. 2018, *ApJ*, 854, 177. doi:10.3847/1538-4357/aaa6b
- Virtanen, P., Gommers, R., Oliphant, T. E., et al. 2020, *Nature Methods*, 17, 261. doi:10.1038/s41592-019-0686-2
- Vlasblom, M., van Dishoeck, E. F., Tabone, B., et al. 2024, *A&A*, 682, A91. doi:10.1051/0004-6361/202348224
- Wilson, T. L. 1999, *Reports on Progress in Physics*, 62, 143. doi:10.1088/0034-4885/62/2/002
- Wright, G. S., Rieke, G. H., Glasse, A., et al. 2023, *PASP*, 135, 048003. doi:10.1088/1538-3873/acbe66
- Xie, C., Pascucci, I., Long, F., et al. 2023, *ApJL*, 959, L25. doi:10.3847/2041-8213/ad0ed9
- Yoshida, T. C., Nomura, H., Furuya, K., et al. 2022, *ApJ*, 932, 126. doi:10.3847/1538-4357/ac6efb
- Yurimoto, H. & Kuramoto, K. 2004, *Science*, 305, 1763. doi:10.1126/science.1100989
- Zhu, X. K., Guo, Y., O’Nions, R. K., et al. 2001, *Nature*, 412, 311